A Satellite Survey of Cloud Cover and Water Vapour in Morocco and Southern Spain and a Verification Using La Palma Ground-based Observations

Final Report

to

European Southern Observatory

By

D. André Erasmus, Ph.D.
(Certified Consulting Meteorologist)
and
Ruby van Rooyen
(Research Assistant)

14 February, 2006

Purchase Order
73526/TSD/04/6179/GWI/LET

TABLE OF CONTENTS

1. Introduction

Two major initiatives to build next-generation extremely large telescopes (ELT) are currently underway in Europe (www.eso.org/projects/owl/) and North America (www.tmt.org). Since the performance of large telescopes at optical and infra-red wavelengths is critically dependent on atmospheric cloud cover and water vapour, it has been recognized that a quantitative survey of these conditions over areas of interest and at candidate telescope sites is and will continue to be an essential part of the site selection process.

Different measurement methods may be used to quantify cloud cover and water vapour at telescope sites but basically there are two categories: ground-based observations and satellite observations. Ground-based observations provide ground-truth for a given site provided the method of observation is reliable. These sites are usually existing observatories where cloud cover is determined using some instrument or a human observer. However, comparable observations are usually not available at potential telescope sites or even many existing sites. In addition, where comparable ground-based data may be available they frequently cover different periods and/or a relatively short period. Further, making similar ground-based measurements at a large number of different sites over a suitably long period of time is logistically impossible.

Meteorological satellites provide a consistent measurement of cloud cover and water vapour over a wide field of view. This allows for a quantitative aerial mapping of relevant cloud cover and water vapour parameters so that a reliable comparison of regions and sub-regions can be made. The spatial (< 10 km) and temporal (3 hours) resolution of the observations also ensures that measurements can be made of conditions at particular sites and that the diurnal cloud cover cycle is resolved. Further, most of the meteorological satellites observing different areas of the globe are equipped with similar instrumentation. This means that areas and sites observed by two or more different satellites can be reliably compared. Satellite data archives now permit a comparison of observing conditions over a reasonably long time period (5 years or more).

Satellite data from the Geostationary Operational Environmental Satellites (GOES-East and GOES-West) have been used to survey cloud cover and water vapour and to conduct comparisons of telescope sites in Northern Chile, the Southwestern USA, Northern Mexico and Hawaii (Erasmus and van Staden, 2001, 2002, 2003). These studies have included comparisons between satellite and ground-based observations at selected sites within the viewing areas of these satellites. Agreement was found to be very good, with the clear fractions obtained using satellite and ground-based observations differing by only a few percent.

In a study for Max Planck Institute (MPI), Heidelberg, satellite data from the Meteosat Indian Ocean Data Coverage Service (in geostationary orbit at 63° east), were used to analyze and compare two sites in the Himalayan region with regard to cloud cover and water vapour (Erasmus, 2004). While it was found that the Meteosat data were well documented and could be processed in a manner similar to GOES data, no comparisons with ground-based observations were carried out.

The area viewed by the Meteosat Operational Service (in geostationary orbit at 0° longitude) includes Africa and Europe (Figure 1). Although a number of existing and potential telescope sites are located in these areas, cloud cover and water vapour conditions have not yet been aerially surveyed and mapped. Developed observatory sites within the viewing area of this satellite include, among others, Observatorio del Roque de los Muchachos (ORM) on La Palma, Calar Alto in southern Spain, Sutherland in South Africa and the Gamsberg in Namibia. Potential observatory sites of high quality may therefore exist in these countries or areas nearby. In terms of a global search for sites for ELTs, therefore, a study of cloud and water vapour conditions over these areas and at specific sites within these areas would be an essential component.

This report presents the results of a study to survey cloud cover and water vapour over Morocco and Southern Spain (including the Canary Islands) using satellite data. This area was identified as the logical starting point for identifying telescope sites in Africa since:

(i) The Canary Islands, located just 300km off the northwest coast of Africa, has well established sites for optical astronomy. Several telescopes have operated at the ORM for a number of years and it is generally regarded as a very good site. For Europe and Northern Africa, therefore, this site would be the logical benchmark against which other sites would be compared and measured. Also, since ground-based observations of cloud cover are available for this site, these can be used to verify the satellite measurements.

(ii) The climate and topography of Morocco and its proximity to the Canary Islands are favourable indicators that potential telescope sites may be found in this area. Much of the area is dominated by subtropical high pressure and a desert climate. Additionally, several mountain peaks of suitably high altitude are found in this region.

For this study cloud cover and water vapour were surveyed over the area 20^oN to 40^oN and 20^oW to 10^oE (Figure 2). In an interim report (Erasmus and van Rooyen, 2004) the preparation and analysis of the satellite data and data from other sources required to perform the cloud cover and water vapour analysis was described and preliminary results showing cloud cover for 1999 and 2000 were presented. In addition, a Technical Supplement (henceforth referred to as TS), containing details on the preparation of the satellite, topography and meteorological data, how the data sets were used in the analysis and development of the analysis algorithms, was submitted with the interim report. This final report contains an overview of the data used (section 2), a description of the methodology and results of the Upper Tropospheric Humidity (UTH) calibration for Meteosat (section 3), results of the area analysis of cloud cover and precipitable water vapour (PWV) using 7 years of data (1996-2002) (section 4), the satellite analysis of cloud cover and the comparison with ground-based observations of cloud cover for the ORM site (section 5) and a description of the database and software package for user-specified cloud cover and PWV analysis within the study area (section 6).

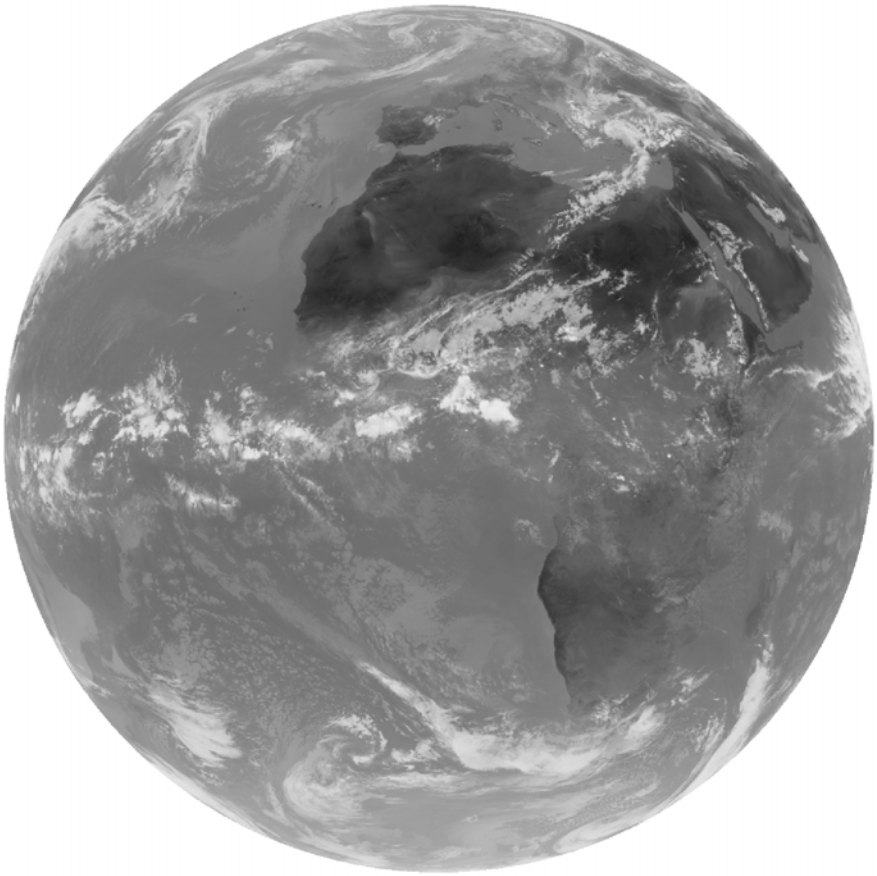

Figure 1. Meteosat Operational Service full earth-disk view at 12 UT on 24 May, 1999 in the infra-red window channel (11.5 µm). © EUMETSAT

Figure 2. Map showing (approximately) the area to be surveyed (20^oN to 40^oN and 20^oW to 10^oE) using Meteosat Operational Service satellite data.

2. The Data

2.1 Satellite data

The satellite data used in this study are from the Meteosat Operational Service in geostationary orbit at 0° longitude (Figure 1). The 6.4µm (water vapour) and 11.5µm (IR window) channel data were analysed to determine cloud cover and water vapour. This study covers the 7-year period January 1996 to December 2002. Data for this period were obtained from the European Organization for the Exploitation of Meteorological Satellites (EUMETSAT) by European Southern Observatory (ESO).

The data were prepared by EUMETSAT for the International Satellite Cloud Climatology Project (ISCCP). The data are the highest spatial resolution prepared for ISCCP (5 km x 5 km at the satellite sub-point) and are stored as rectified full earth disk images in a format called IDS OpenMTP (TS, Chapter 2).

Preparation of the satellite data involved an intensive evaluation of the full disk images to check for errors (TS, section 2.1). Rectification errors (distortions) were observed in images capturing eclipse events and images with missing South Pole area data. Distortion errors are very rare and were found to be in only 24 images over the 7 year period. Scanner errors leading to missing (black) or saturated (white) scan lines or pixels were also found but these are frequently limited to a small fraction of the image. While these were found to be more frequent than distortion errors they could be dealt with dynamically in the analysis by testing the value of each pixel against a reference mean or neighbourhood mean.

The next step in preparing the satellite data was extraction of sectors containing just the data for the study area. This makes the data volume more manageable and speeds up data processing. A system was developed whereby the sectors extracted from the full disk images could be repacked in the same image format, namely IDS OpenMTP, with the necessary calibration and navigation information (TS, section 2.2 and 2.3). A sample image of the extracted sector is shown in Figure 3.

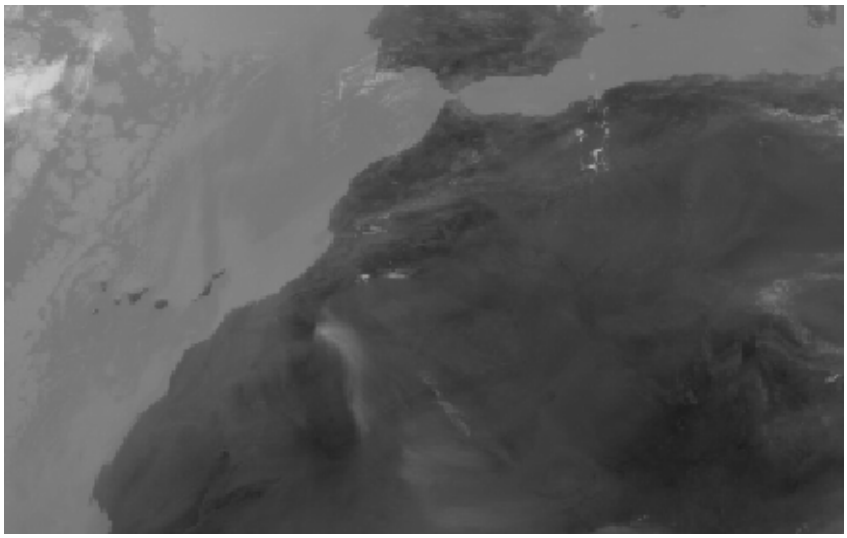

Figure 3. Sample image (12UT on 24 May, 1999) of the sector extracted from the full-disk Meteosat data (see Figure 1).

For the data used in the ORM site analysis an additional extraction of the site pixel data was performed. A 9-pixel area was used to represent the site (see section 3).

2.2 Topography data

Terrain heights over the area of interest are needed in order to estimate surface temperature and pressure from the rawinsonde or gridded meteorological data used in the analysis (see section 2.3). This information is used to differentiate between cloud above the surface and the ground. Terrain height data in digital format were obtained from the Global 30 Arc-Second Elevation Data Set (GTOPO30) (edc.usgs.gov/products/elevation/gtopo30.html) and data for the sector 20°N to 40°N and 20°W to 10°E were extracted. Since the topography data is higher resolution (~ 1 km) than the satellite data, the terrain height for any given satellite pixel location was deemed to be the highest point within the area (~ 5 km x 5 km) covered by the pixel (TS, Chapter 3). Figure 4 shows a grey-scale map of the study area topography.

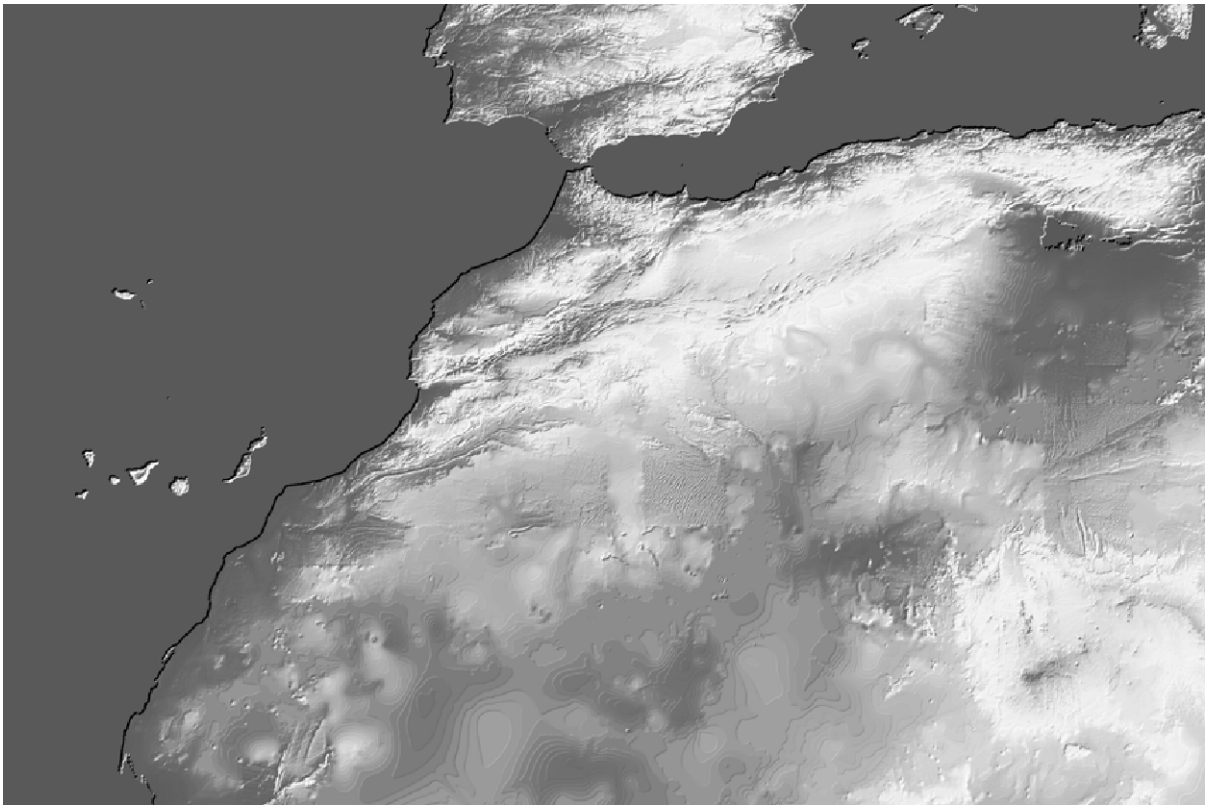

Figure 4. Greyscale map of the study area topography. Higher terrain is lighter and the ocean is a uniform dark grey.

2.3 Meteorological data

In order to determine the presence of cloud in the IR window channel imagery and to derive an absolute humidity from the satellite-derived relative humidity, a measurement of the temperature profile above the ground is required. This measurement may be obtained from rawinsonde soundings or gridded numerical meteorological model reanalysis data. Rawinsonde data were also used to perform the UTH calibration for Meteosat.

2.3.1 Rawinsonde data

Balloon-borne instrument packages are released from stations around the globe at standard times (00UT and 12UT) each day. The sensor packages transmit data on atmospheric pressure, temperature and humidity to a ground station. As the balloon ascends and drifts with the wind, it is tracked by radio theodolite or the Global Positioning System (GPS) to determine its position. From the position data and pressure-altitude relationships, wind speed and direction are obtained as the balloon ascends.

Archiving of the rawinsonde data after real-time use is undertaken by a number of organizations and institutions at their discretion. The most comprehensive archives are kept by the Forecast Systems Laboratory (FSL) of the National Oceanographic and Atmospheric Administration (NOAA) of the U.S.A. (raob.fsl.noaa.gov/) and by the U.S.A. National Climatic Data Centre (NCDC). The NCDC archive has the longer historical record while FSL hosts a web-accessible active archive with data from 1998 onward.

The two archives list about 19 rawinsonde stations in the area of interest that have data. However, only 10 stations have reasonably good data coverage over the study period (Table 1).

Table 1. Rawinsonde stations in the study area with reasonable data coverage over the study period

Station Name	Latitude	Longitude	Altitude
PALMA	39.55	2.62	6
MURCIA	38.00	-1.17	62
GIBRALTAR	36.15	-5.33	3
FUNCHAL	32.63	-16.90	56
LISBON/GAGO	38.77	-9.13	105
SANTA CRUZ de TENERIFE	28.47	-16.25	36
CASABLANCA/ANFA	33.57	-7.67	62
AL MASSIRA	30.33	-9.42	74
DAR-EL-BEIDA/HOUARI	36.72	3.25	25
BECHAR/OUAKDA	31.62	-2.23	773

The 10 sites are shown in Figure 2 with white station name labels. It is clear that spatial coverage over the area is generally poor. In addition, it was observed that, even for these 10 stations, there are significant (1-12 month long) data gaps between 1996 and 2002. In view of the inadequate temporal and spatial coverage of the rawinsonde data and the need to process a large percentage (> 95%) of the satellite images it was decided not to use the rawinsonde data in the aerial analysis and mapping of cloud cover and water vapour. For the UTH calibration and for the analysis of site conditions at the ORM on La Palma the rawinsonde data for the Santa Cruz de Tenerife station were used since a sub-period with good data coverage could be selected for these applications.

2.3.2 NCEP-NCAR reanalysis data

The National Center for Environmental Prediction (NCEP) and National Center for Atmospheric Research (NCAR) reanalysis data set is a retroactive reconstruction of atmospheric parameter fields (Kistler *et al*, 2001). Historical data from all possible sources were collected and added to existing databases. Data then underwent an extensive quality control. An assimilation scheme, kept constant over the reanalysis period, was then used to interpolate the observations to a global grid. For each year a data CD of selected atmospheric parameter fields is produced at 2.5^{o} x 2.5^{o} in the horizontal for one or more times per day. Vertical resolution depends on the parameter. Meteorological data for the area of interest were extracted from the global NCEP-NCAR reanalysis data set (TS, Chapter 4).

The data fields and parameters selected for possible use in the analysis were:

2 m temperature (00UT and 12UT)
2 m minimum temperature (daily)
2 m maximum temperature (daily)
850 mb temperature and geopotential height (00UT and 12UT)
500 mb temperature and geopotential height (00UT and 12UT)
200 mb temperature and geopotential height (00UT and 12UT)

The manner in which the data were used in the analysis is described in section 3.

3. Methodology

In this study measurements of cloud cover and water vapour are derived from satellite observations by passive remote sensing at different wavelengths. Depending on the wavelengths being measured by the satellite, different quantities can be derived. The meteorological data obtained from the NCEP-NCAR reanalysis are used to provide an independent temperature measurement. This is needed to facilitate the detection of clouds and the computation of the PWV. Further, information on the terrain height at each pixel location is needed so that cloud can be discriminated from the ground and the mistaken detection of elevated cold surfaces as cloud can be avoided. The merging of these three data sources and their respective grids was described in TS Chapter 5. Details on implementation of the methodology described here were presented in TS, Chapter 6.

3.1 Definitions of seasons and day/night divisions

The analysis was performed for different seasons and periods of the day. Seasons were defined on a climatological basis as follows:

Winter	-	December, January, February (DJF)
Spring	-	March, April, May (MAM)
Summer	-	June, July, August (JJA)
Fall	-	September, October, November (SON)

Day/night divisions are based on true solar time or local mean time. The computational method is similar to that of Sarazin (1991) which is based on the *Guide to Meteorological Instruments and Methods of Observation, Annex 9D, World Meteorological Organization* (1983). The elevation angle of the sun (h_o) is given by the equation:

$$\sin h_o = \sin \delta * \sin \varphi + \cos \delta * \cos \varphi * \cos t \qquad (3.1)$$

where δ is the declination of the sun for a given day of the year, φ is latitude and t is the solar angular time counted from midday.

δ is given by:

$$\delta = 0.006918 - 0.399912\cos\theta + 0.070257\sin\theta + 0.006758\cos 2\theta + 0.000908\sin 2\theta \qquad (3.2)$$

where θ is the annual solar angular time given by:

$$\theta = 2\pi d_n/365 \qquad (3.3)$$

and d_n is day of the year.

At sunrise and sunset $h_o = 0$, thus for any given day of the year, one can solve for t in equation 3.1. At the equinoxes, t is exactly π/2 radians, which corresponds to 6 hours in time. Thus, for any given day of the year and latitude the equivalent time in hours before and after midday is given by t * 6 * 2/π.

Local apparent time (LAT) is then given by

$$LAT = GMT + LC + Eq, \qquad (3.4)$$

Where GMT is Greenwhich Mean Time, LC is a longitude correction of 4 minutes for every degree and Eq, the equation of time, is a correction to obtain apparent (true) solar time from mean solar time.

$$Eq = 0.0172 + 0.4281\cos\theta - 7.3515\sin\theta - 3.3495\cos 2\theta - 9.3619\sin 2\theta \qquad (3.5)$$

In the area analysis, the solar time is computed for each pixel location separately. In the analysis that follows, “Night” is defined as the period starting at true local sunset time to true local sunrise time with “Day” defined analogously. A strict definition of the astronomical night was not applied since this ensured that all the available satellite images are processed including those near sunset and sunrise. This makes sense meteorologically since cloud cover conditions at and about the time of sunset and sunrise would be representative of conditions during the intervening night. Further divisions into day1, day2, night1 and night2 are done by dividing the applicable period exactly in half.

3.2 Synchronization of satellite and NCEP-NCAR data

Satellite images are available every 3 hours at 00UT, 03UT, 06UT, 09UT, 12UT, 15UT, 18UT and 21UT while the NCEP-NCAR reanalysis data are available twice daily at 00UT and 12UT. Given the timing of these observations in relation to the diurnal cycle of temperature, the closest NCEP data time is not necessarily the best choice. For the study area 00UT observations are near mid-night and 12UT observations near mid-day. In terms of temperature, conditions between sunrise and about two hours thereafter would be better represented by the 00UT data than the 12UT data. Accordingly, when synchronising the satellite and NCEP data, the 00UT NCEP data are used for satellite images between sunset + 2 hours and sunrise + 2 hours and the 12UT NCEP data for images between sunrise + 2 hours and sunset +2 hours.

3.3 Principles of satellite measurement

The satellite data used in this study are measurements of the monochromatic emittance of the earth and atmosphere at 11.5μm and at 6.4μm. Figure 5 shows the weighting functions for different satellite infra-red observing channels. In the IR window channel (11.5μm), emissions reach the satellite largely unattenuated by the atmosphere so that radiance values measured are due to emission from the surface. However, clouds absorb and emit essentially as blackbodies at infra-red wavelengths. The result is that when clouds are present in the atmosphere, they behave as an elevated emitting "surface" so that radiation reaching the satellite is from the cloud top. By using an independent temperature measurement the cloud top height can be determined.

Figure 5 indicates that satellite observations at 6.4 μm are sensitive to atmospheric emissions from the layer between about 600mb (~ 4400 m) and 300mb (~ 9000 m). These emissions are from resident water vapour. Therefore, the satellite observation channel near 7 μm is commonly referred to as the water vapour (WV) channel. If high altitude (cirrus) clouds exist above this layer they would absorb the outgoing radiation and re-emit to space at colder temperatures. Thicker clouds absorb more of the radiation from the lower atmosphere. The presence and thickness of cirrus cloud can therefore be determined from the WV channel data.

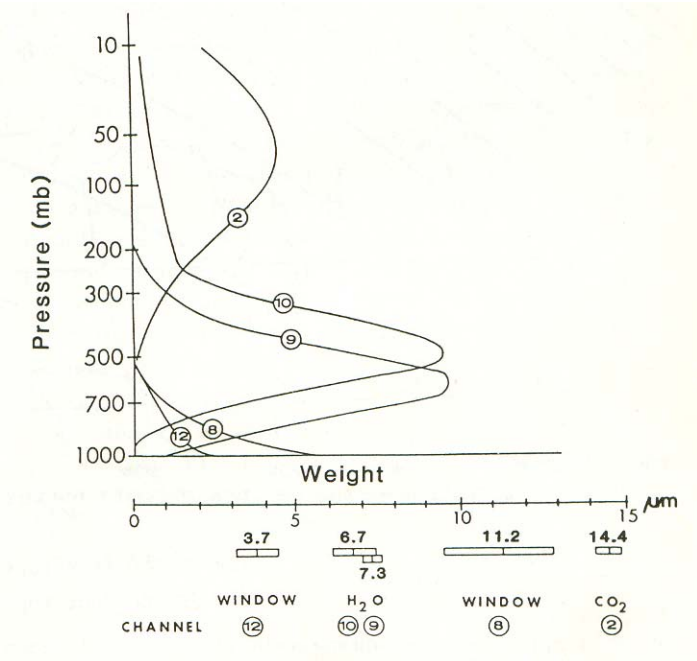

Figure 5. Weighting functions for selected infra-red observing channels (from Rao *et al.*, 1990)

3.4 Conversion of radiance counts to radiance and brightness temperature

In the real-time (raw) data stream for Meteosat radiance counts are 10-bits in length for the imager channels. In order to maintain compatibility with older data sets such as Meteosat-3, these have been scaled into 8-bit counts for ISCCP. The conversion from channel count to radiance is given by:

$$R = \alpha(C_n - C_0) \quad [Wm^{-2}sr^{-1}] \qquad (3.6)$$

where R = radiance,
α = calibration coefficient ,
C_n = 8-bit radiometer count ,
C_0 = space count.

The calibration coefficient (α) is defined for various channels and provided by EUMETSAT (www.eumetsat.de/en/dps/mpef/calibration_mfg.html).

The relationship between radiance and brightness temperature is defined by the Planck function and may be written as:

$$R = \exp [A + (B/T)] \quad [Wm^{-2}sr^{-1}]$$

where T = brightness temperature [K]
A = dimensionless regression coefficient,
B = regression coefficient [K]
R = radiance

The coefficients A and B are defined for each satellite observing channel and are supplied by EUMETSAT (www.eumetsat.de/en/dps/mpef/temp-rad_conv.html).

3.5 Conversion of 6.4µm brightness temperature to UTH

The Upper Tropospheric Humidity (UTH) is a measure of the relative humidity of a layer extending approximately from 600 mb to 300 mb. For GOES data, Soden and Bretherton (1993, 1996) have derived a semi-empirical relationship between UTH and water vapour channel brightness temperature (T_{wv}) in clear areas. They used simplified radiative transfer theory to define the following logarithmic relationship between UTH and the brightness temperature:

$$UTH = [\exp(a + b*T_{wv}) * \cos\theta] / p0 \qquad (3.7),$$

where θ is the satellite viewing zenith angle, a and b are the least squares fit slope and intercept of the regression line as defined by the empirical relationship and p0 is a normalized pressure variable.

$$p0 = p(T=240K)/ 300, \qquad (3.8)$$

where p (in mb) is the pressure level where the temperature (T) is 240K. The factor p0 accounts for the lifting (lowering) of the weighting function peak in warm (cold) airmasses.

The values for a and b are seasonally dependent and determined for each month of the year (See wwwghcc.msfc.nasa.gov/irgrp/ulhumidity_tech.html).

For Meteosat-5 a calibration for UTH was performed in a similar manner using rawinsonde data from selected sites in the study area. Since the main area of interest for this study is the subtropics, the rawinsonde stations used in the calibration were chosen accordingly. Table 2 lists the stations used in the calibration.

Table 2. Rawinsonde stations used in the calibration of UTH for Meteosat-5

WMO ID	Station Name	Latitude	Longitude	Altitude (m)
08301	PALMA DE MALLORCA	39.55	2.62	6
08430	MURCIA	38.00	-1.17	62
08495	GIBRALTAR	36.15	-5.33	3
08522	FUNCHAL	32.63	-16.90	56
08579	LISBON/COUNTINHO	38.77	-9.13	105
60020	SANTA CRUZ de TENERIFE	28.47	-16.25	36

In the calibration procedure T_{wv} is obtained for the pixel location corresponding to the rawinsonde station using the satellite image which is closest in time to the rawinsonde sounding. Only clear days are used and observations are required to be within one hour of each other. When the UTH is derived from the sounding, the raw temperature and dew point data are first interpolated to pressure surfaces at 25 mb increments. Then the mixing and saturation mixing ratio is obtained at each level and the relative humidity is computed using the method in Erasmus (2005). Finally the weighting function for the Meteosat-5 water vapour (6.4µm) channel for a dry subtropical atmosphere is applied and the weighted UTH is determined (Figure 6). MATLAB was used to obtain the relationship between T_{wv} and UTH using least squares regression.

In performing the calibration, the rawinsonde data were checked for consistency over time and from one station to the other. A discontinuity was observed starting in June 1998 (Figure 7). Accordingly only data from 1999-2002, covering three full annual cycles, were used in the calibration. To check consistency between stations the calibration coefficients were computed for each station separately. Using the relationships thus derived, the UTH was obtained for a fixed brightness temperature for each month of the year (Figure 8). It is readily apparent that aberrant UTH values are observed in the month of July for Santa Cruz and Gibraltar and in January, April and November for Funchal. These aberrations are caused by a scarcity of data in the months and locations mentioned. At the other four rawinsonde stations such irregularities are not observed since data coverage is adequate for all months of the year. This check shows that it is unwise to base the UTH calibration on just one station (such as Santa Cruz de Tenerife, for example). Consequently for the UTH calibration, data from all the stations listed in Table 2 were used. The final calibration coefficients are shown in Table 3. The scatter and regression line plots for each month are shown in the Appendix.

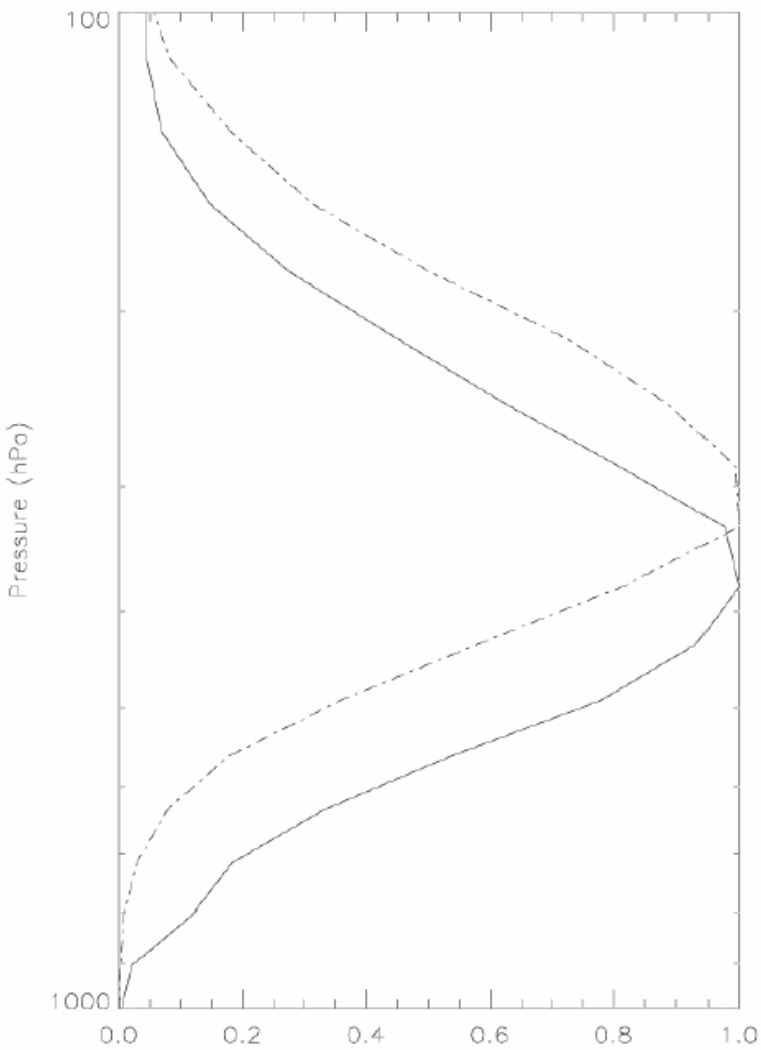

Figure 6. Weighting functions for the Meteosat 5 water vapour (6.4µm) channel. The dotted curve is for a moist (RH=70%) profile and the solid line for a dry (RH=20%) profile. In both cases, in the boundary layer (between 1000mb and 800mb) the RH is set to 80%. (from Roca *et al.*, 2003).

Table 3. UTH calibration coefficients derived for the Meteosat-5 water vapour (6.4µm) channel.

Month	Intercept	Slope	Correlation Coef
January	-0.11117	30.27163	0.74152
February	-0.11832	32.15065	0.82154
March	-0.12479	33.64035	0.78709
April	-0.11227	30.62167	0.75077
May	-0.10037	27.79913	0.71975
June	-0.11566	31.40630	0.78211
July	-0.11780	32.01875	0.72845
August	-0.11985	32.54142	0.74006
September	-0.10158	27.92453	0.73952
October	-0.11322	30.83951	0.71921
November	-0.12638	34.00080	0.81486
December	-0.11346	30.87666	0.76124

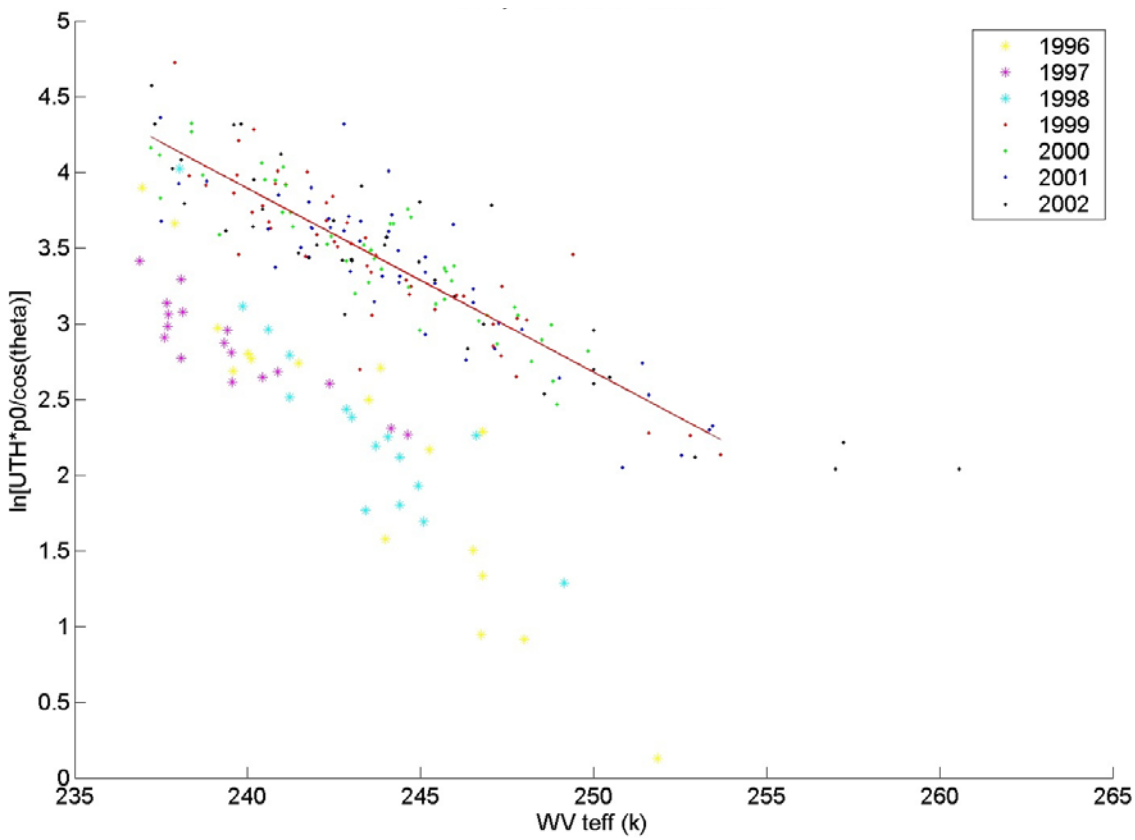

Figure 7. Calibration data for February showing the discontinuity in data prior to June 1998.

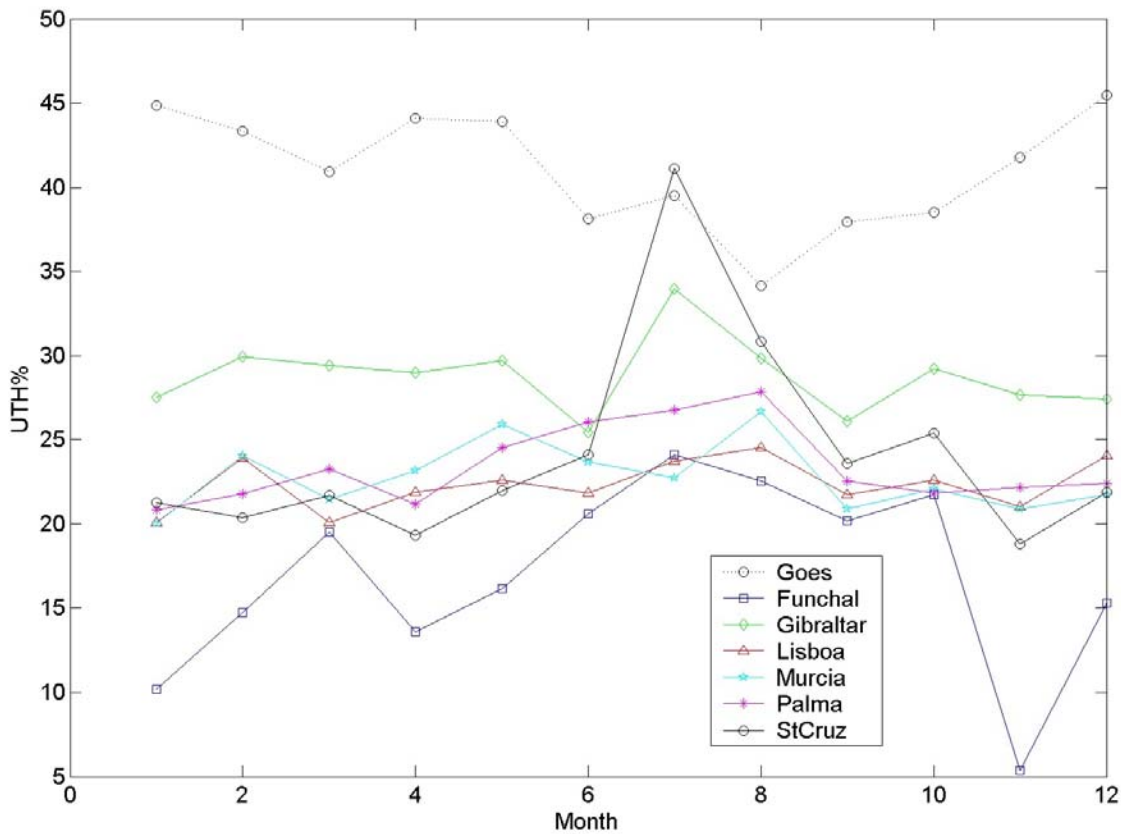

Figure 8. UTH corresponding to a fixed reference T_{wv} obtained using calibration coefficients derived for each station separately.

3.6 Conversion from UTH to PWV

The precipitable water vapor (PWV) is a quantity indicating the absolute humidity in the atmosphere above some predetermined altitude such as the surface or a constant pressure level. It is derived from the satellite-based UTH measurement. Since the UTH is a measure of the relative humidity in the layer between 300mb and 600mb, for pressure levels between 300mb and 600mb the relative humidity is set equal to the UTH. Then the corresponding mixing ratio (x), the mass of water vapor per mass of air (Kg/Kg), at each level (25mb increments were used) can be computed as follows:

$$x = UTH \cdot x_s \qquad (3.9).$$

x_s, the saturation mixing ratio, is the maximum water vapor carrying capacity of the air at a given temperature and pressure. In the area analysis, it was computed using the temperature versus height (pressure) profile derived from the NCEP-NCAR data (see Figure 10). In the site analysis for ORM, rawinsonde data for Santa Cruz de Tenerife was used.

The next step in the computation of PWV is deriving the mixing ratio values for pressure levels below 300mb and above 600mb. Figure 9 shows the average mixing ratio profiles for four months in the year as derived from the Antofagasta rawinsonde. The profiles exhibit good linearity with pressure (height) from the 850mb pressure level upwards. It is also clear that the contribution to total PWV from levels above 300mb is very small. To obtain the unknown mixing ratio values, the computed values for 300mb and 600mb respectively were scaled to lower and higher pressure levels. In the area analysis this was done by linear extrapolation. For the site analysis scaling was done using the moisture profile from the rawinsonde sounding for the closest station and time.

Once the mixing ratio profile is obtained, then,

$$PWV = (1/g) \int_{o}^{p} x.dp \qquad (3.5)$$

where dp is the incremental pressure change with height in Pascals and g is the gravity acceleration constant. The units for PWV are then $kg.m^{-2}$ or mm of water.

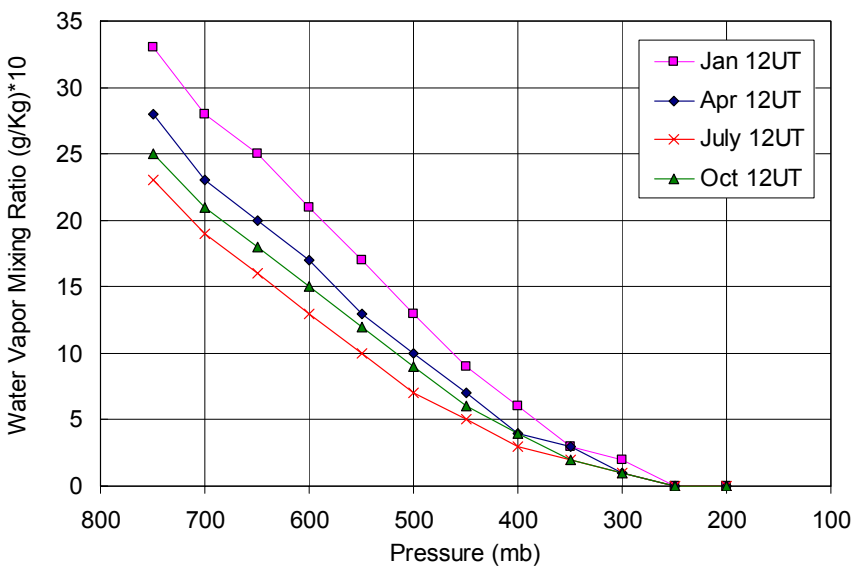

Figure 9. Mean monthly water vapor mixing ratio versus pressure (height) profiles as determined from the Antofagasta rawinsonde for the 10 year period 1977-1986.

3.7 Cloud detection and classification

The presence of cirrus (high altitude) clouds and their thickness is inferred from the 6.4μm imagery. These clouds are found at an altitude (9-12km) which is higher than the water vapour emission layer. The cloud particles absorb radiation from below and emit to space at relatively cold temperatures. The thicker the cloud, the lower will be the brightness temperature measured by the satellite. The relationship between UTH and water vapour brightness temperature defined in section 3.5 is applicable under clear conditions. When UTH values rise to around 50%, cirrus cloud particles start forming by condensation and deposition (the cloud particles may not be visible at this stage or have any effect on optical transparency). As UTH values rise further, the cloud particles grow in size and number and the cirrus cloud gets thicker.

The relationship between UTH, cirrus cloud thickness and atmospheric extinction at optical wavelengths has been investigated by Erasmus and Sarazin (2000, 2002). Atmospheric extinction measurements made by the *Line Of Sight Sky Absorption Monitor* (LOSSAM) at La Silla Observatory over a 9-month period were compared to a transparency index based on the satellite UTH measurement. It was found that the transparency index correctly discriminated between photometric and non-photometric conditions 86% of the time. In a more recent comparison (Erasmus *et al.*, 2003), based on two years of LOSSAM and satellite data for both Paranal and La Silla Observatories, similar results were obtained with photometric and non-photometric conditions correctly discriminated 91.5% and 83% of the time at the two sites, respectively. In the last study, the satellite-based extinction parameter was an explicit function of the UTH. For different ranges of UTH values the probability of encountering photometric versus non-photometric conditions could therefore be computed using the corresponding frequencies of occurrence. Since the findings were remarkably similar for both sites, the tallies were combined. The results are shown in Table 4.

Table 4. Number (first column) and percentage (second column) frequency of occurrence of photometric and non-photometric conditions for different ranges of UTH values as observed at Paranal and La Silla Observatories over the period October 1999 to September 2001.

	UTH (%)							
Observing quality	< 30		30-50		50-80		80-100	
Photometric	1953	97.5	316	79.8	94	56.3	2	9.1
Non-photometric	51	2.5	80	20.2	73	43.7	20	90.9

If the UTH is less than 30% there is a 97.5% probability of conditions being photometric. When the UTH is between 80% and 100% then the probability that conditions will be non-photometric is over 90%. For all cases with UTH greater than 100% (opaque clouds) no LOSSAM measurement could be made, thus indicating that conditions were unusable. When the UTH is between 30% and 80% cirrus clouds of variable thickness (hence transparency) may be present and observing conditions could be either photometric or non-photometric.

It should be noted that the information presented above on the relationship between UTH and optical transparency is based on GOES data. It can not be said with

certainty that the same results would be obtained using Meteosat data. In deciding which UTH threshold values to use to discriminate between photometric, non-photometric but usable and unusable conditions in this study it was therefore decided to differentiate the categories as strictly as possible.

Accordingly the following categories and threshold values were used:

Clear (photometric): UTH ≤30%
Transparent (spectroscopic): 30%<UTH<100%
Opaque (unusable): UTH ≥100%

The Infra-red windows (11.5μm) channel data were used to detect cloud in the middle and upper troposphere. In principle the procedure for cloud detection is straightforward. Pixel temperatures (T_{ir}) computed from the 11.5μm satellite data need to be referenced against an independent temperature measurement. Typically, temperature drops with height in the atmosphere, so if T_{ir} is colder (by some margin) than the surface temperature (for example) at a given pixel location, the presence of cloud above the surface is indicated. In practice, however, there are some obstacles to the task of unambiguous cloud detection.

As a first step towards determining the cloud detection temperature threshold (T_r) with which T_{ir} must be compared, the surface pressure (P_s) and corresponding surface temperature (T_s) for a given location may be estimated using the rawinsonde sounding data (or NCEP-NCAR reanalysis data) and the terrain height. Given the altitude of the surface and the geopotential heights of the pressure levels, P_s and T_s can be estimated by interpolation from the vertical temperature profile. (Figure 9).

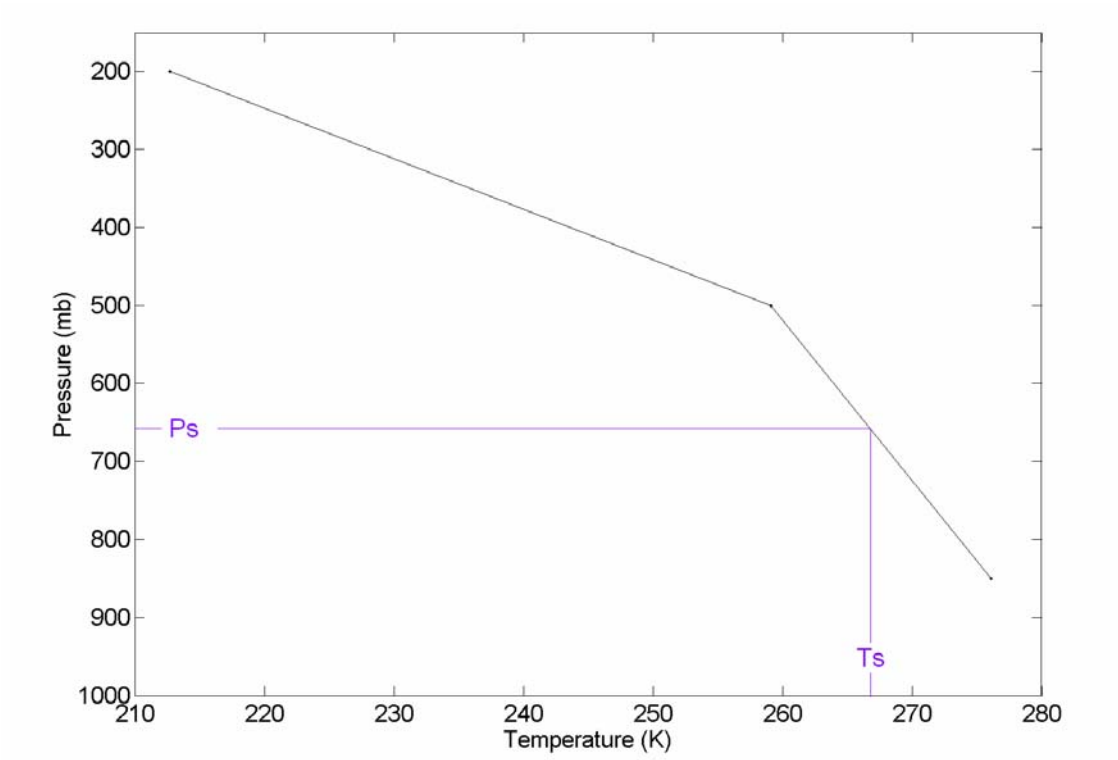

Figure 10. Example of the vertical profile of temperature derived from the NCEP-NCAR reanalysis data as used in the area analysis of cloud cover.

However, the actual surface temperature may be warmer or colder than T_s since there is usually additional cooling (night) or warming (day) of the air near the ground. If the estimated surface temperature is cooler than the actual surface temperature (daytime) cloud detection is not compromised. If cloud is present (even a thin layer near the surface) during the daytime, the cloud top temperature (T_{ir}) will be colder than the estimated surface temperature. So if $T_r = T_s$, cloud is correctly determined to be present. However, if the actual temperature is colder than the estimated surface temperature (T_s) and $T_{ir} < T_r = T_s$, then two conditions are possible - cloud may be present or the ground is cold and is incorrectly being interpreted as cloud. In order to avoid this problem a T_r must be used that is lower than T_s when the actual surface temperature is colder than T_s. At the same time the difference between T_r and T_s must be minimized so that cloud, if it is near the ground, does not go undetected.

The ground detection problem described above necessitates the definition of an exclusion zone directly above the surface in which cloud can not be detected (Figure 11). For the *aerial analysis* a generally applicable method for defining the depth of the exclusion zone is needed. Erasmus and van Staden (2002), in surveying the Southwestern U.S.A. and Northern Mexico, developed a method that parameterises the depth of the exclusion layer in terms of night length and time elapsed between sunset and the satellite observation time (the length of time the ground has cooled). Parameterisation was based on data for a selection of sites representing the range of ground detection effects to be found over the area to be mapped. A logarithmic function was used to define the relationship between the depth of the exclusion layer and hours of cooling after sunset.

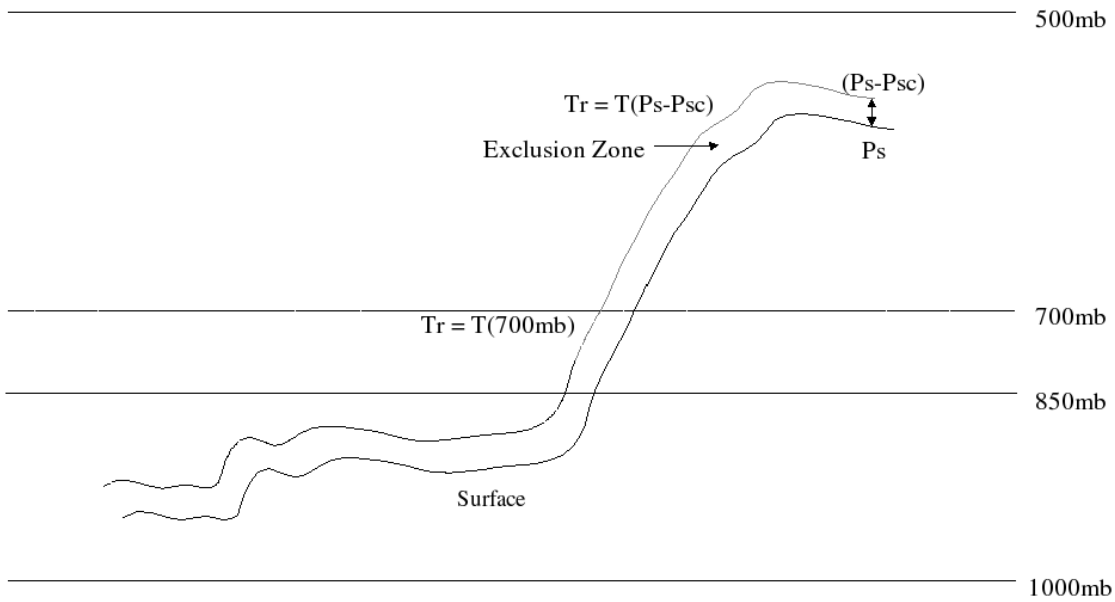

Figure 11. Schematic diagram showing the relationship between the terrain height and the threshold temperature for cloud detection (T_r) as applied in the area analysis of cloud cover.

This method, while it was generally successful in dealing with the ground detection problem, has two disadvantages:

(i) Nocturnal cooling effects were assumed to end suddenly in the early morning. This caused a sudden step-wise change in the depth of the exclusion layer at the transition.

(ii) The highest terrain points, where ground detection is generally a greater problem, were not necessarily included in the sites used to define the logarithmic function. So the exclusion layer was unnecessarily deep in some locations and too shallow in others.

An improved methodology for defining the depth of the exclusion layer in the area analysis of cloud cover has been developed and applied in this study. Mistakenly detecting ground as cloud is most likely over higher terrain in the winter months. Since the main area of interest for finding new potential telescope sites in this study is the Atlas Mountains, the high terrain area used to define the exclusion layer covers the area 30.6696^{o}N to 33.7415^{o}N and 3.7469^{o}W to 8.8659^{o}W. Pixel locations where the corresponding terrain height is greater than 2500m were identified. In total 563 pixel locations were used. For the 6-week period 1 January to 15 February (coldest weeks in winter), over the years 1999 to 2001, a visual examination of satellite images was made and days or parts of days that were cloud free over the highest terrain were identified. A sequence of three or more clear images was sought and all satellite image scan times during the day were sampled. When processing these images, known to be clear, the threshold temperature for cloud detection (T_r) was set equal to the surface temperature (T_s). For each pixel with a terrain height greater than 2500 m, the terrain height, T_{ir}, T_s, P_s and the gradient of temperature with pressure (height) (dT/dP) were output to files for each image.

The quantity $T_r - T_{ir}$ was computed for all pixels. If this quantity is positive ground is being detected in that pixel. For pixels with $T_r - T_{ir} > 0$ the mean and standard deviation of ($T_r - T_{ir}$) was computed. A temperature offset (delT) is defined as follows:

$$\text{delT} = \text{mean}\ (T_r - T_{ir}) + 2\ [\text{standard deviation}\ (T_r - T_{ir})] \qquad (3.9)$$

Subtracting an offset of delT from T_r implies that for 95% of the pixels in that image, ground detection would be avoided. The equivalent pressure offset (thickness of the exclusion layer) is then given by:

$$\text{delP} = \text{delT} / \text{mean}\ (dT/dP) \quad [\text{mb}] \qquad (3.10)$$

where mean (dT/dP) is the average for all pixels in the high terrain area. (dT/dP does not vary significantly over the high terrain area since it is defined using the NCEP-NCAR data which has 2.5^o x 2.5^o resolution).

delP was computed in this manner for each of the clear images and then statistics of the delP values were complied for each satellite image scan time. Figure 12 shows the mean, 75th percentile and 90th percentile values for delP for each satellite image scan time. If the delP values corresponding to the 90th percentile curve are used to define the thickness of the exclusion layer, ground detection is avoided in 90% of the selected (mid-winter) images under clear conditions. This was selected as a suitably strict criterion for avoidance of mistaken ground detection. A cubic spline was fitted to the data and the equation for this spline is used to define the depth of the exclusion layer (P_{sc}) for any given time of the day. Over lower terrain, defined as being locations where $P_s - P_{sc} > 750$mb, the temperature at the 750 mb pressure level is used to define T_r in the area analysis.

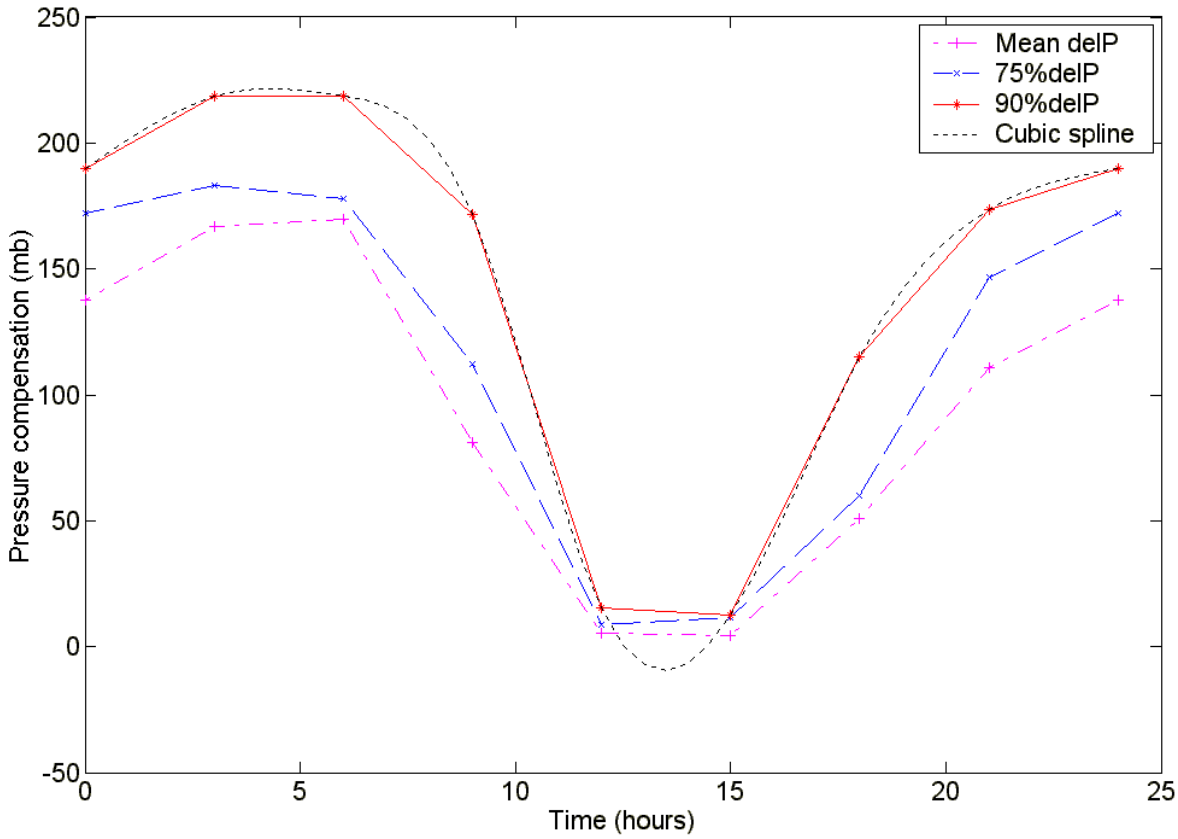

Figure 12. Plots (different confidence levels) showing the pressure compensation needed to avoid mistaken detection of cold ground as cloud over high terrain at the coldest time of the year for different times of the day. The fitted cubic spline is used to define the thickness of the exclusion layer in the area analysis of cloud cover.

The procedure for cloud detection in the analysis employed in this study used observations made at both 6.4µm and 11.5µm. First, the 6.4µm imagery were used to determine the existence of transparent or opaque cirrus at high altitude. If a pixel is determined to have opaque cirrus then the final cloud cover classification for that pixel location was “opaque”. However, if a pixel is either clear or transparent from the 6.4µm image analysis, the corresponding pixel in the 11.5µm image was examined. If cloud is detected in that pixel then the pixel location was classified as opaque. If not, then pixel locations classified respectively as clear or transparent remain clear or transparent.

Rather than using just one pixel to represent the “sky” above a particular location, a cluster of pixels was used. As shown schematically in Figure 13, a 9-pixel area may be used to represent the astronomical sky. At the level of the Tropopause (about 12km), for an observer on the ground viewing the sky, this 9-pixel area would correspond to the sky within approximately 45° of zenith for the Meteosat ISCCP data used in this study. Individual pixels were classified as clear, transparent or opaque and then the counts for each category were used to classify the observing conditions for the astronomical sky. The following scheme was used in the area analysis performed for this report:

Clear (Photometric): All 9 pixels are clear
Transitional (Spectroscopic): 6-8 pixels are clear (1-3 pixels are transparent or opaque)
Opaque (Unsuitable for astronomy): 5 or fewer pixels are clear

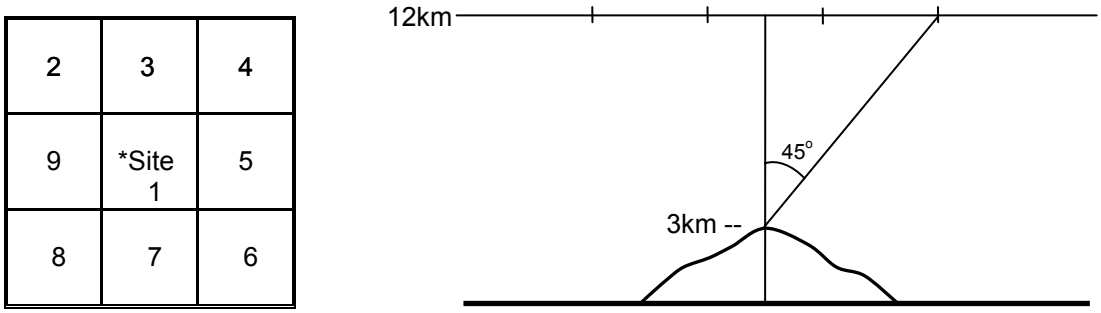

Figure 13. Schematic diagram showing the 9-pixel site area in plan view (left) and cross-section (right). At left, each square represents a pixel (~ 6 km x 6km) in the satellite image. At right, assuming a site altitude of 3km, at Tropopause level (approximately 12km), the "sky" encompassed by the 9-pixels corresponds approximately to an area of observation within 45° of zenith.

4. Results

4.1 Area Analysis: Cloud Cover

For the study area covering Morocco and Southern Spain (including the Canary Islands) (20°N to 40°N and 20°W to 10°E) satellite data for the period 1996 to 2002 were processed and aerial maps showing the distribution of clear skies were constructed using GrADS (grads.iges.org). The maps were compiled using the sky cover categories for the 9-pixel area centered on each pixel location in the study domain as defined in section 3.7. The frequency of occurrence of each sky cover category was counted for each pixel location, expressed as a percentage frequency and then isokephs (lines joining places with equal frequency of occurrence. fr. G. *isos*, equal, and *kephalaion*, sum) were drawn. The maps presented below show the clear fraction (%) for the 7-year period overall, by season and for different times of the day. All maps produced, including the transitional (spectroscopic) and opaque (unusable) fractions may be found on the CD accompanying this report.

It is important to note that the clear fractions are derived using individual images 3 hours apart. Thus, for a given pixel location the clear fraction is the count of clear signatures divided by the total number of images processed. The fraction of clear nights will be lower. For example, if 6 or more hours of clear skies are required for a night to be considered clear, then a sequence of 3 or more images per night would need to be clear.

4.1.1 Overall conditions

The map showing the distribution of clear skies for night-time hours over the 7-year period 1996-2002 is shown in Figure 14. The map indicates that the latitudinal maximum for the clear fraction occurs at about 28°N. At this latitude there is only a slight west to east gradient with the clear fraction dropping about 5% over the land areas compared to the ocean. The clear fraction drops to the north and south of this latitude. In addition, increases in cloud cover of about 15% are observed over the highland areas of the Atlas Mountains and the Ahaggar Plateau (southern Algeria) compared to locations at a similar latitude further west over the ocean. This increase occurs because mountains are preferred areas for cloud development by convection, particularly in the summer months (see Figure 16). In addition, at other times of the year, cloud cover is enhanced by orographic lifting of the air stream over these highland areas. The map also shows that the clearest locations in the Atlas mountains are those located furthest south and west, *i.e.* in the Anti-Atlas range.

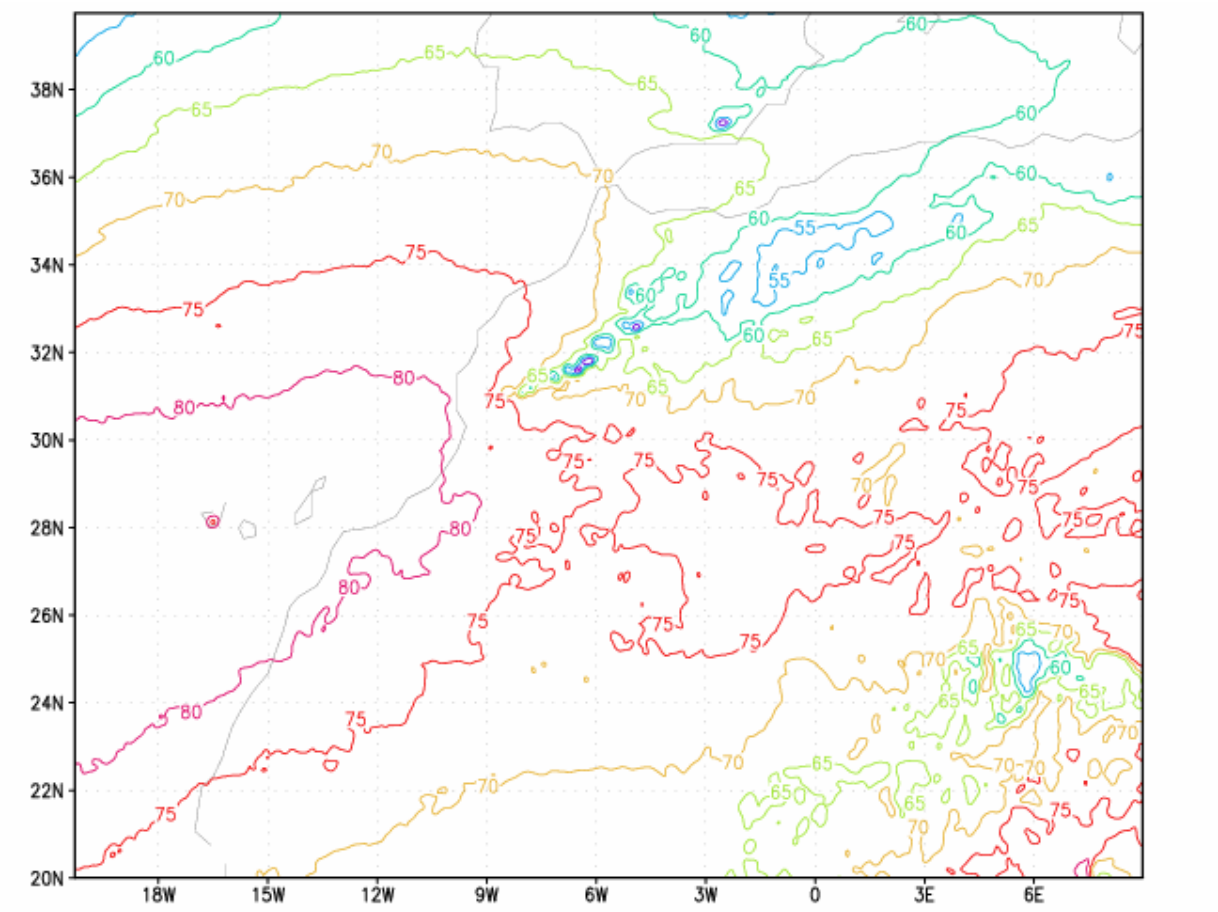

Figure 14. Fraction of time that skies are clear (%) at night over the period 1996 to 2002.

4.1.2 Seasonal variations

Maps showing the clear fraction for the four seasons defined in section 3.1 are presented in Figures 15 - 18. These reveal the same general pattern as observed in the overall map. In addition, the maps show that the latitude belt with the clearest skies migrates northwards in summer and southwards in winter. This is consistent with the seasonal movement of the subtropical high pressure region. Over the Atlas Mountains and the Canary Islands, cloudiness is greatest in winter. This is due to the more southerly path and greater strength of cyclones and fronts at this time of the year. The enhancement of cloud cover over the highland areas due to the development of convective storms is seen most clearly on the Summer map. At other times of the year the mountainous areas also experience greater cloudiness. Convection and orographic lifting of the air over these areas are responsible for this increase. (Note: In the south-east corner of the Winter map (Figure 18), a highly complex isokeph pattern is observed in the vicinity of the Ahaggar Plateau. Since the primary area of interest in this study was Morocco and Southern Spain, the ground detection avoidance algorithm was optimised for these areas. Most likely, therefore, ground detection is the cause of the isokeph pattern observed in and around the Ahaggar highlands. Interestingly, closer examination of this area reveals that the higher terrain is largely unaffected (the 70% clear area at 23°N, 5°E coincides with higher topography). In winter, inland desert valleys are, in fact, colder than the surrounding higher terrain due to cold air drainage into these valleys. Apparently, these cold valleys, which show up as “cloudy” in this area at this time of the year, are producing the observed isokeph pattern.)

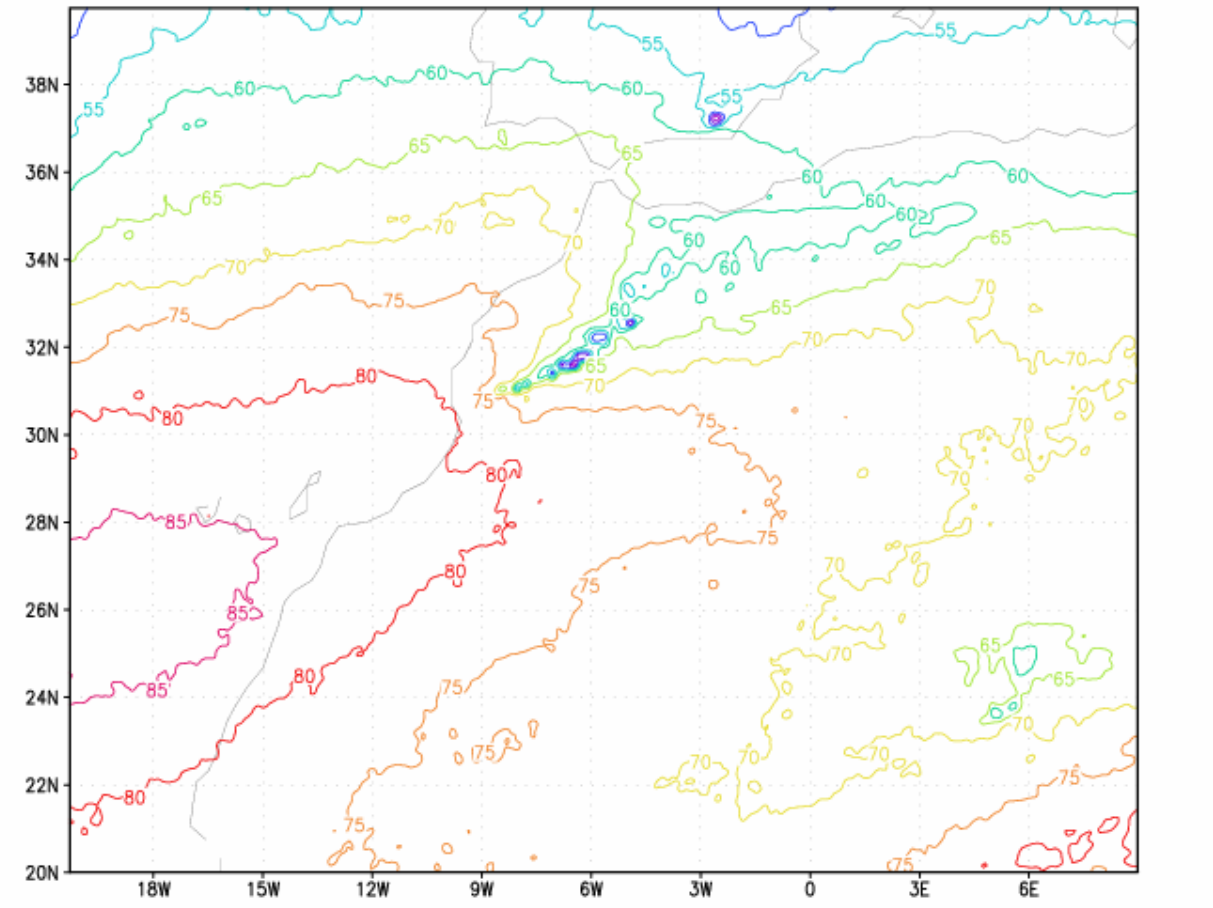

Figure 15. Fraction of time that skies are clear (%) at night in Spring (1996-2002)

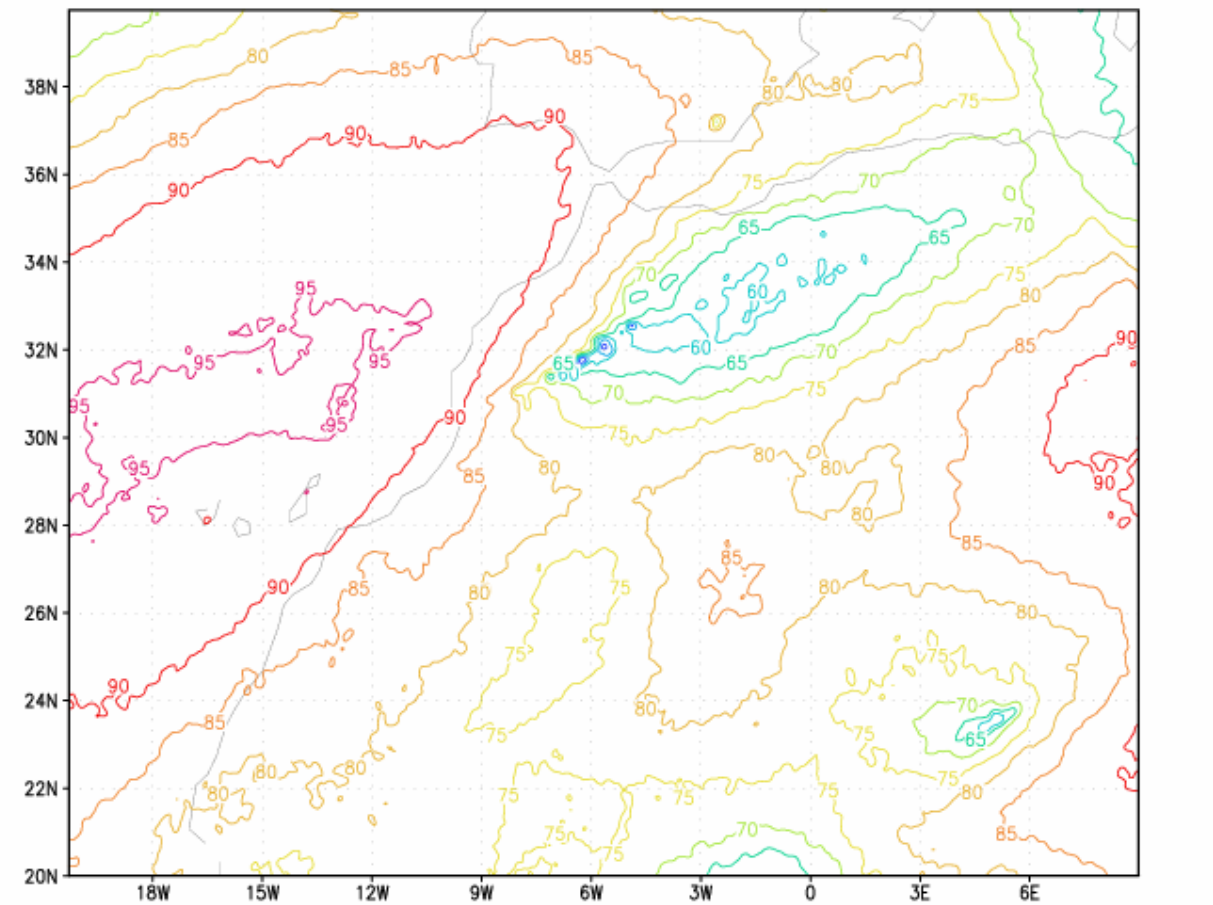

Figure 16. Fraction of time that skies are clear (%) at night in Summer (1996-2002).

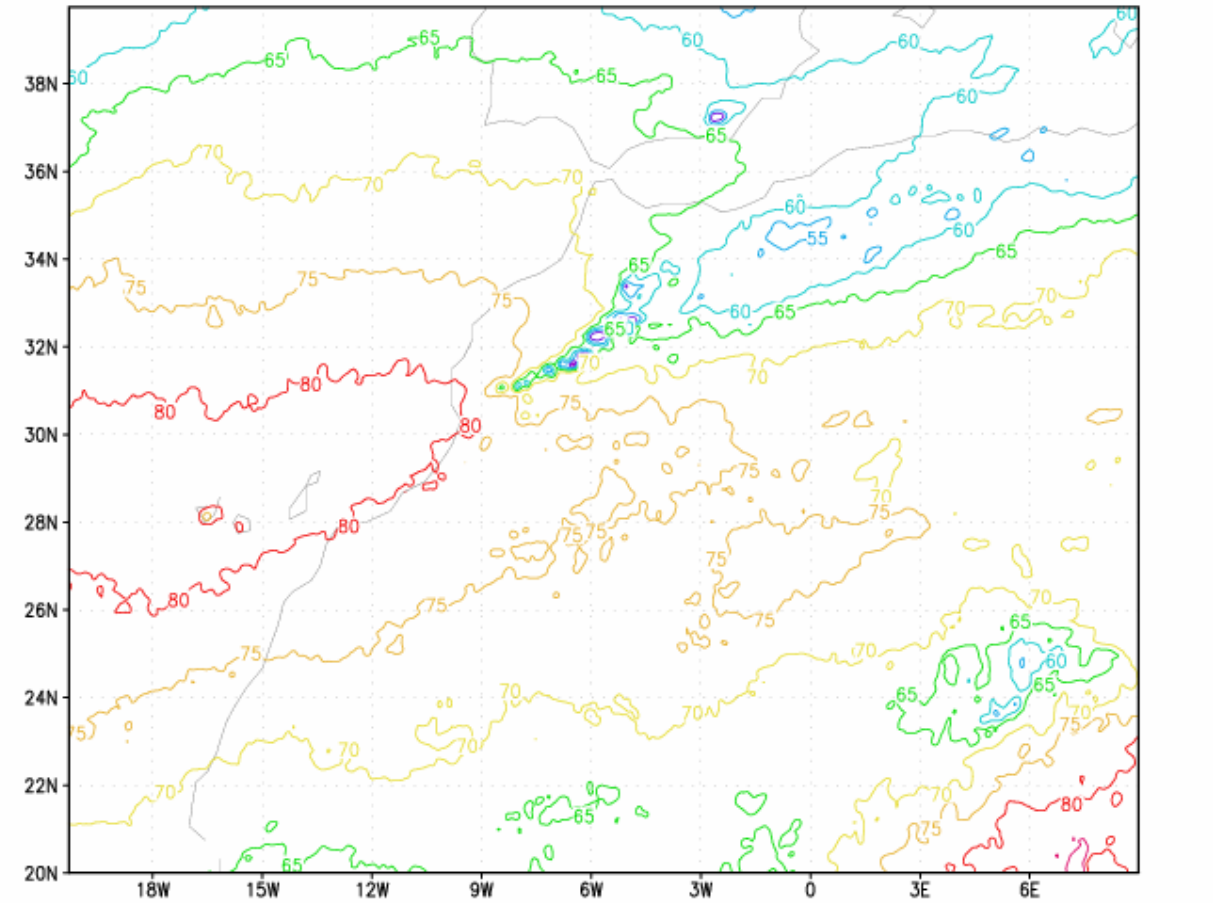

Figure 17. Fraction of time that skies are clear (%) at night in Autumn (1996-2002).

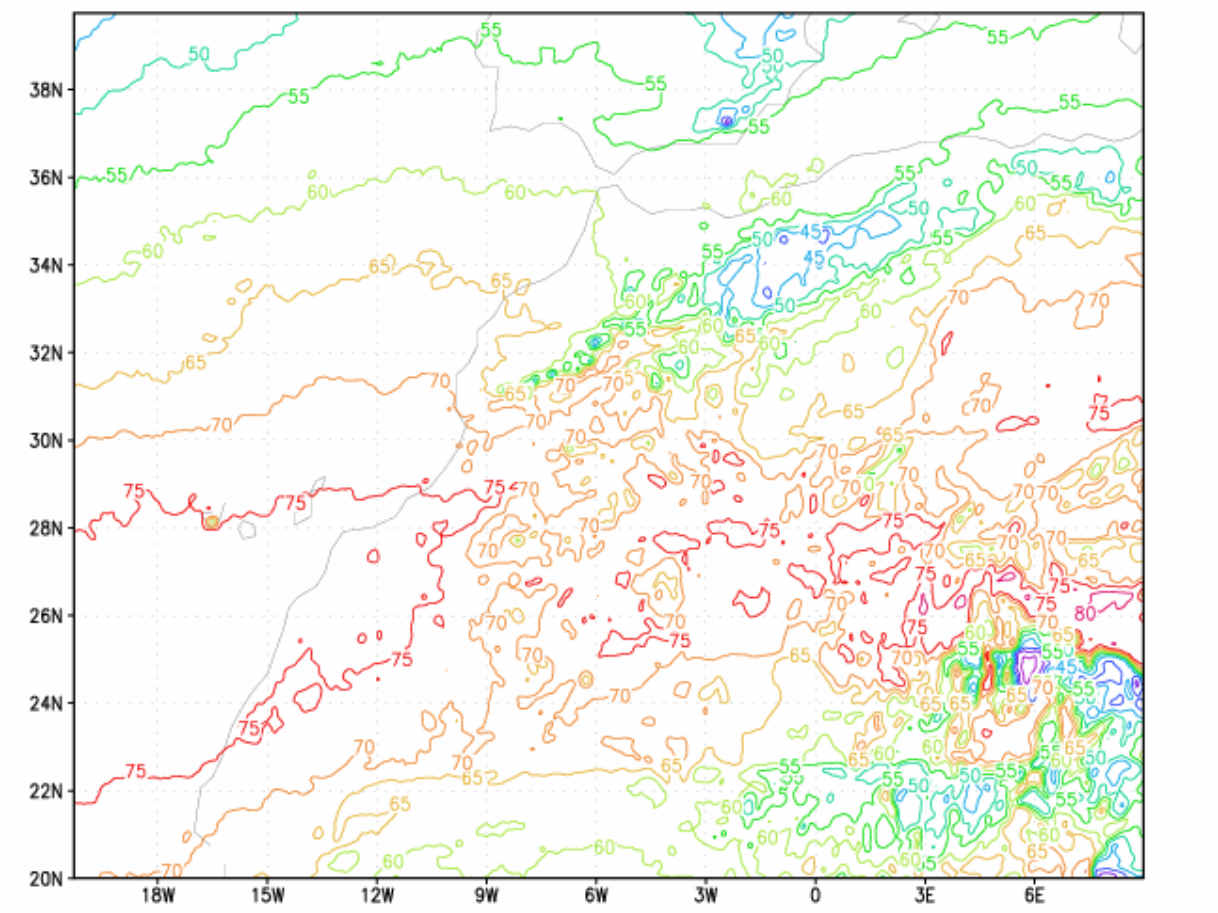

Figure 18. Fraction of time that skies are clear (%) at night in Winter (1996-2002).

4.1.3 Diurnal variations

Maps showing the distribution of the clear fraction for the four day-night periods defined in section 3.1 are shown in Figures 19 - 22. Diurnal variations in cloud cover are small over the ocean and coastal areas and larger over inland areas. This is consistent with the fact that the oceans moderate the daily cycle of temperature, an important control for diurnal cloud cover variations. Daily variations in cloud cover are particularly noticeable over the high terrain areas which show a significant increase in cloud cover in the second half of the day. This is caused by convective cloud (thunderstorm) development in the afternoon hours which dissipates at night. The convective cycle of cloud cover is particularly noticeable in the south-western part of the Atlas mountains. In the north-eastern Atlas the daily cycle of cloud cover is less dramatic showing that orographic effects are more important than convection in this region. In the Ahaggar highlands in the second half of the night when the ground is very cold the complex isokeph pattern discussed in section 4.1.2 is again observed.

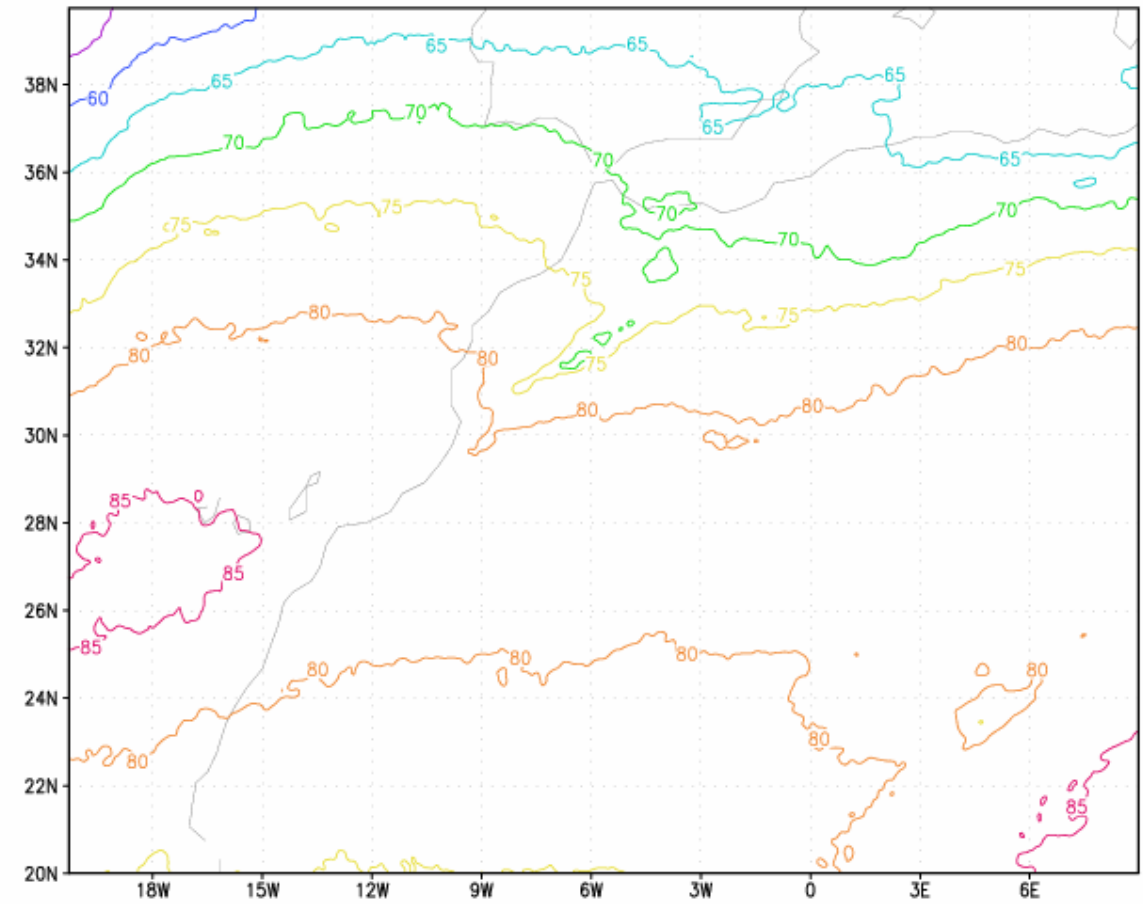

Figure 19. Fraction of time that skies are clear (%) during the first half of the day (1996-2002).

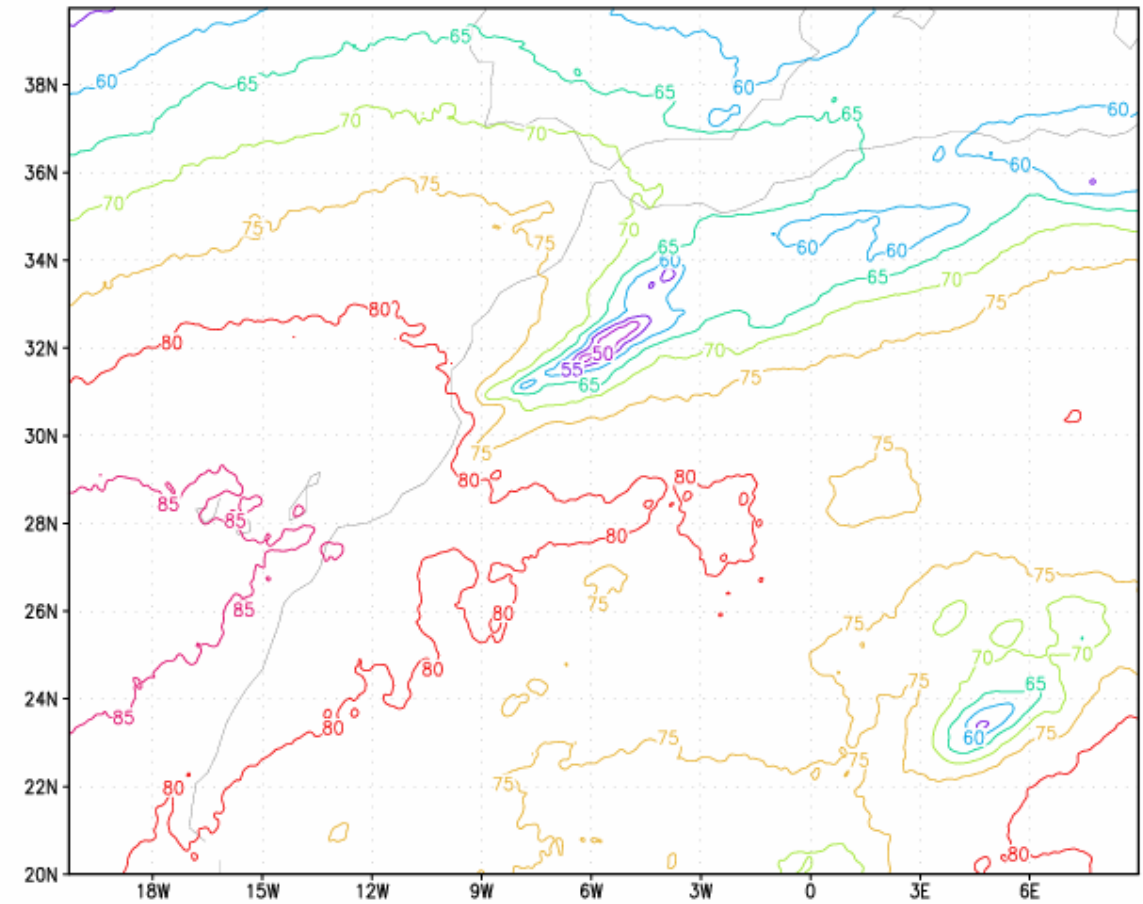

Figure 20. Fraction of time that skies are clear (%) during the second half of the day (1996-2002).

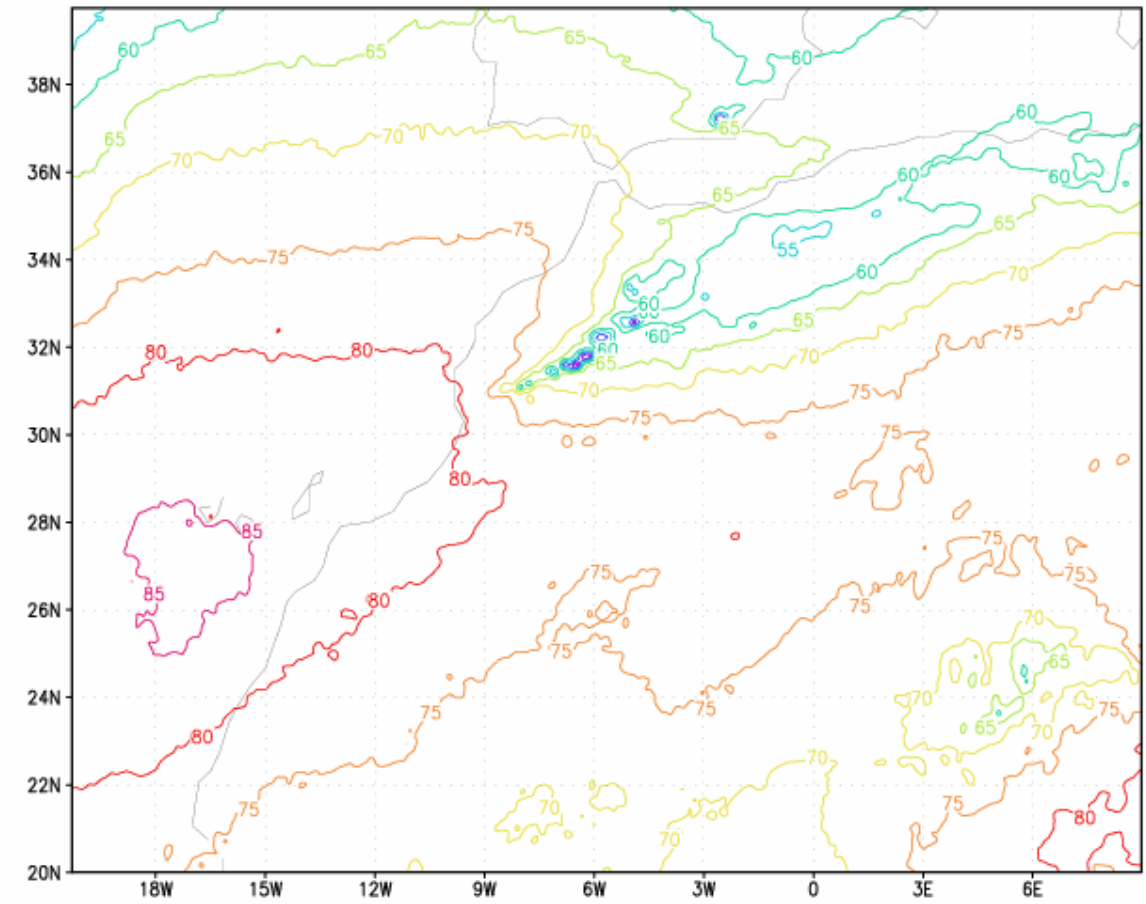

Figure 21. Fraction of time that skies are clear (%) during the first half of the night (1996-2002).

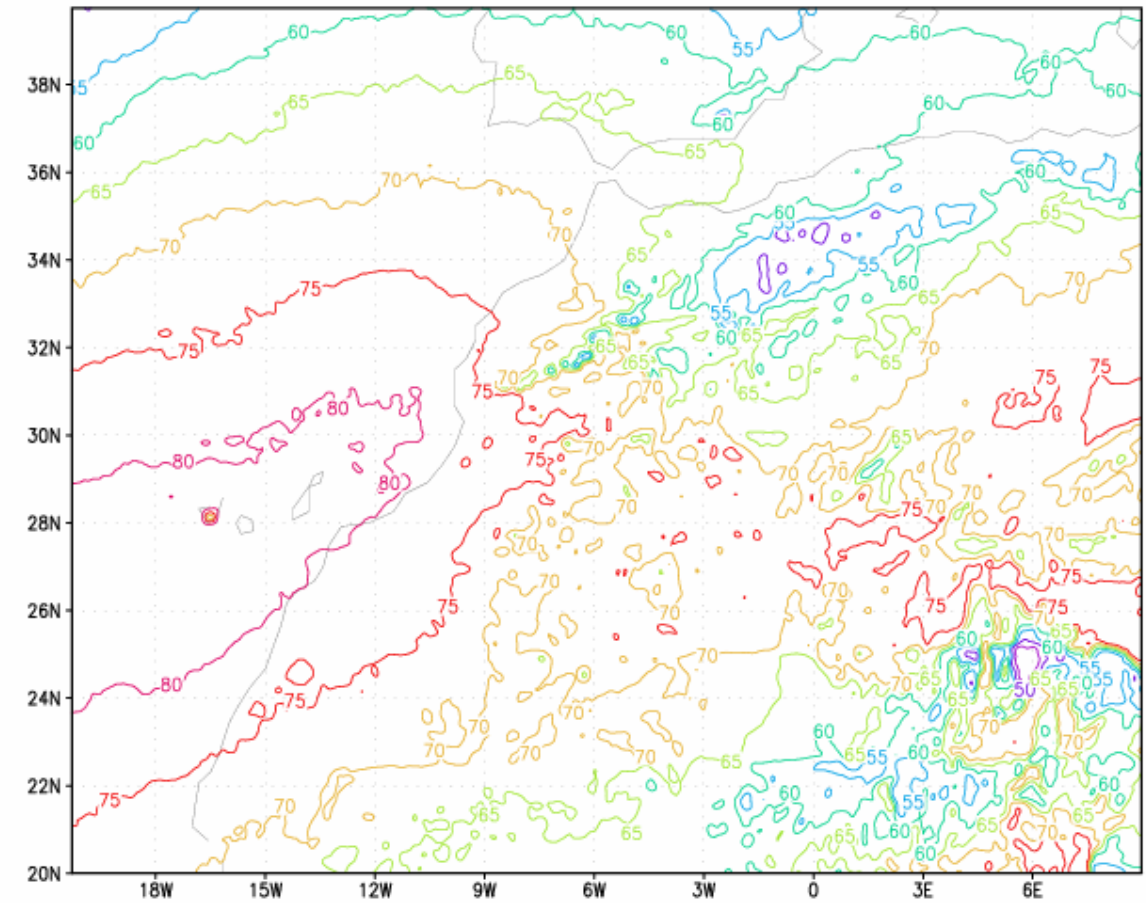

Figure 22. Fraction of time that skies are clear (%) during the second half of the night (1996-2002).

4.2 Area Analysis: PWV

Maps showing the distribution of PWV over the study area (20°N to 40°N and 20°W to 10°E) for the period 1996 to 2002 are presented below (Figures 23 – 25). The figures show isokeph plots of the percentage frequency of occurrence of PWV values below selected thresholds, namely, 1 mm, 2 mm and 3 mm respectively. The plots are for PWV in the atmosphere above the 750 mb pressure level (~ 2500 m). Where the terrain is higher than this pressure level, PWV is for the atmosphere above the surface.

The isokephs on the PWV maps exhibit linear ramp-like characteristics in certain areas. These artefacts are most noticeable in areas where moisture levels are low and where the upper-air meteorological data used to derive the PWV from the satellite measurement is sparse. As noted in section 3, the NCEP-NCAR upper-air data used in the analysis has a resolution of 2.5° x 2.5° in the horizontal. Section 2.3.1 shows that rawinsonde data coverage over the area is relatively poor, being worst over the inland areas of north-west Africa. Since rawinsonde data is the primary upper-air data input to the NCEP-NCAR temperature data reanalysis, horizontal temperature variations in this area would be poorly resolved in the NCEP-NCAR data. Since latitudinal temperature variation is generally significantly larger than longitudinal variation in the atmosphere, the latter is particularly poorly resolved in the area in question. This temperature resolution problem spills over into the computation and hence plotting of PWV. The tropics are an exception. Even though upper-air data quality is equally poor in this area, the moisture signal (from the satellite) is strong and spatial variations in water vapour are significant. Because this is the case, variability in the satellite-derived PWV field can be detected and resolved even though the upper-air temperature field is poorly resolved.

A number of methods were used in an attempt to reduce the effects of the problematic upper-air temperature data on the appearance of the PWV isokephs. The basic method of using the NCEP-NCAR temperature data was to compute a bi-linear interpolation using the four grid points closest to the satellite image pixel. To reduce the linear artefacts, grid point values in the north-south direction were biased (various weights were tried) and/or additional grid points were used. In addition, smoothing using various mask sizes was applied. Removing the offending lines (apparently at 2.5° intervals) manually from the data prior to plotting was also tried but this simply causes the lines to move one pixel north or south. All the methods tried yielded similar results. Thus it was concluded that the problem with the quality of the upper-air temperature data and its effect on the PWV isokephs could not be addressed simply by using post-processing methods. The *effective* spatial resolution of the upper-air temperature data is poor in a large part of the study area.

Since diurnal and seasonal variations in PWV are very small, only the maps for overall conditions are shown below. As is the case with cloud cover the water vapour minimum is found at about 28°N latitude. This is consistent with drying of the air as it subsides in the subtropical high pressure region. There is little variation from west to east across this latitude belt. Moisture levels increase to the north and south of the subtropics. This is the case since these areas experience more disturbed weather events which inject moisture found near the surface into the middle and upper troposphere. The spatial pattern observed is consistent for all three of the PWV thresholds used.

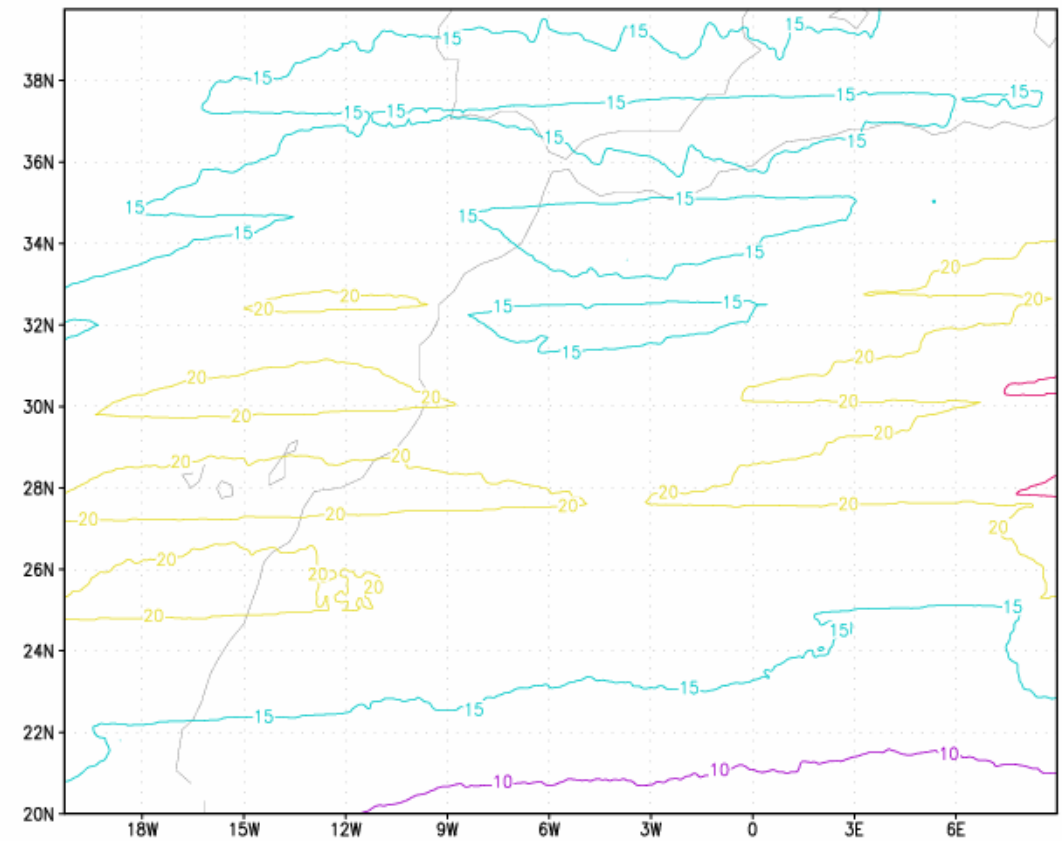

Figure 23. Percentage frequency of occurrence of PWV values below 1 mm over the period 1996 – 2002.

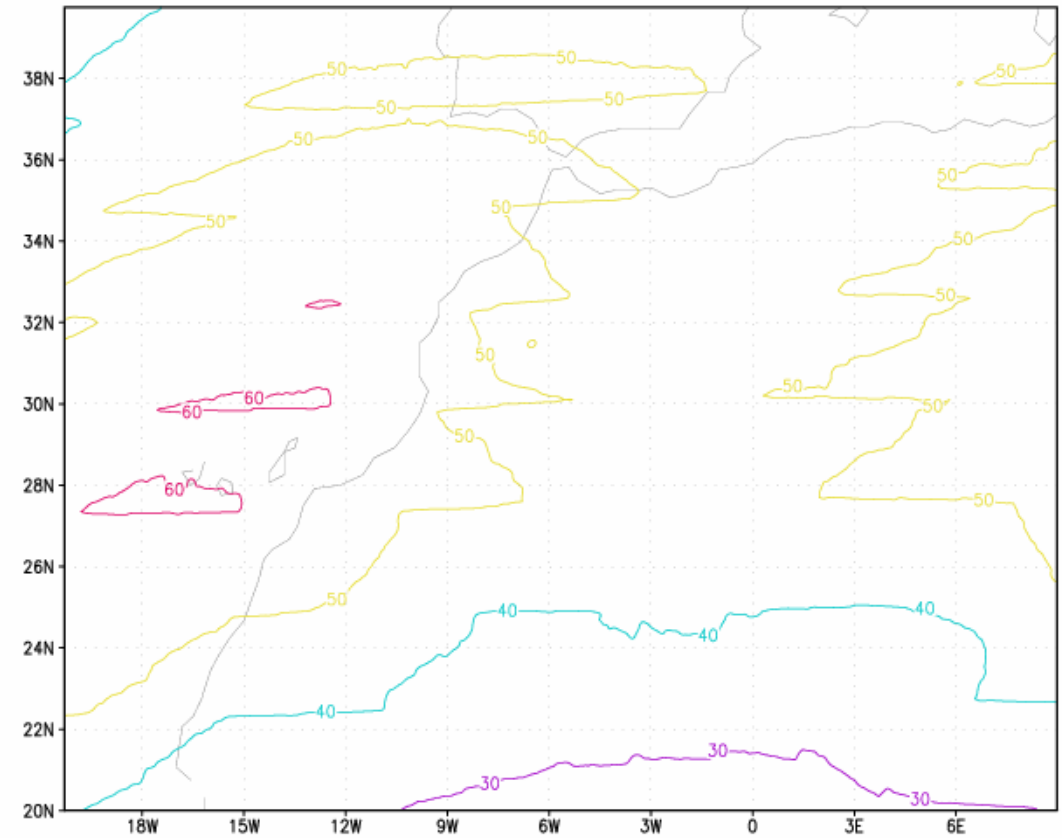

Figure 24. Percentage frequency of occurrence of PWV values below 2 mm over the period 1996 – 2002.

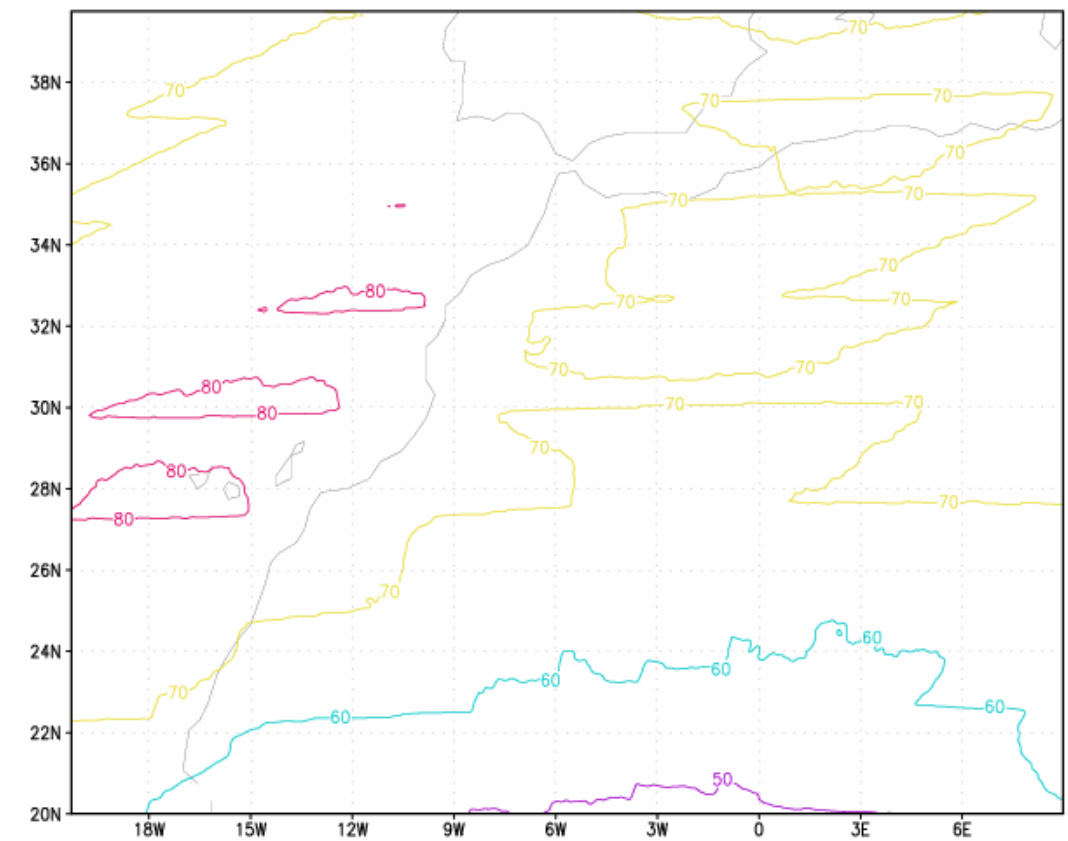

Figure 25. Percentage frequency of occurrence of PWV values below 3 mm over the period 1996 – 2002.

The altitude dependence of PWV does not show up clearly in Figures 23 – 25 because the terrain areas above the 750mb pressure level (~2500 m) are small, because smoothed digital elevation model terrain heights are used in the area analysis and, additionally, because the isokephs have been smoothed. In the unsmoothed PWV plots found on the CD accompanying this report, the highest terrain areas in the Atlas mountains with low PWV values may be identified in the 1 mm threshold plot.

5. ORM site analysis and comparison with ground observations

In order to verify the accuracy of the satellite observations of cloud cover, these were compared to ground-based observations made at the Observatorio del Roque de los Muchachos (ORM). The ground-based observations used to determine sky cover conditions were made by the Carlsberg Meridian Telescope (CMT). The CMT uses about 50 photometric standards per night to determine atmospheric extinction. Then the number of hours of photometric data and non-photometric data were determined. These records are provided by CMT on their web page (www.ast.cam.ac.uk/ ~dwe/SRF/camc_extinction.html). Using this information, the *nightly photometric fraction* was determined for each night by dividing the number of photometric hours by the total number of hours observed.

The same fraction was computed using the satellite data. The observing night was defined to be the period of the day when the sun was more than 9 degrees below the horizon. Using satellite images for the observing night, the nightly clear fraction was computed by counting the total number of clear pixels in each image using the 9-pixel site designation and dividing by the total number of possible pixels. At least 3

images per night were required otherwise the night was excluded from the comparison. The satellite nightly clear (photometric) fraction is a spatio-temporal average and so partly clear sky coverage is included (eg. In a given satellite image only some of the 9 pixels may be clear). This actually corresponds well to what is considered to be a “photometric” sky in the CMT measurements since for these only a limited part of the sky is required to be photometric (Evans, 2005). In both cases, since partly clear skies are allowed, the clear or photometric fraction is, in effect, the usable (photometric plus spectroscopic) fraction.

In processing the CMT data it was found that, on a number of nights, the sum of the photometric and non-photometric hours is significantly less than the night length. Unfortunately it was not possible to determine if these hours were “lost” due to technical problems, weather-related events or simply because observations were not made through the whole night. Therefore, when comparing the CMT data to the satellite it was decided to limit the comparison to nights where the total number of CMT hours observed was at least 80% of the night length.

The nightly clear (photometric) fractions were compared using the nights for which both CMT and satellite data were sufficient. 629 nights in the period 1999-2002 were used. Time series plots showing the clear/photometric fractions for individual nights are presented in Appendix B for the years 2000-2002 (The plot for 1999 is omitted since there are only 48 nights with simultaneous data in 1999). Nights were compared by defining three sky cover categories for the night as follows:

Photometric:	Clear/Photometric fraction greater than 90%
Spectroscopic:	Clear/Photometric fraction between 50% and 90%
Unusable:	Clear/Photometric fraction less than 50%

Table 5 shows the counts for each combination of categories as determined by the satellite and the CMT measurements respectively. Defining a “Hit” as complete agreement, “Neutral” as disagreement by one category and a “Miss” as complete disagreement the following rates are determined from the data in Table 5:

Hit:	66.1%
Neutral:	28.0%
Miss:	5.9%

In terms of the difference between the satellite and ground-based measurements, there is no strong bias towards either method. The satellite overestimates the clear fraction by one category on 80 nights relative to the ground measurement and the ground measurement overestimates the clear fraction by one category on 96 nights relative to the satellite measurement. The corresponding number of nights for overestimation by two categories is 16 and 21 respectively. Taking night length into account, the clear/photometric hours were computed for the 629 nights and divided by the possible hours. The fraction of photometric time, including time when only part of the sky was photometric, was found to be 83.7% and 85.3% for the satellite and ground-based observations respectively.

Given the differences in the measurement methods, the timing of observations and the constraints applied in the comparison (as described above), the satellite and ground-based measurements were found to be in remarkably good agreement.

Table 5. Counts of nights in different observing categories as determined from satellite and ground-based observations.

		Satellite		
Ground		Unusable	Spectroscopic	Photometric
	Unusable	34	17	16
	Spectroscopic	15	52	63
	Photometric	21	81	330

6. Software package for cloud cover and PWV analysis

A software package accompanies this report which allows a user to analyse cloud cover and/or PWV over an area of interest or at a particular location within the study domain. The RPM package and documentation is being delivered to ESO under separate cover. Factors related to the appropriate use of this software are discussed in this section.

Users must bear in mind that the basis for the analysis in the software package is the area analysis of cloud cover and PWV described in section 3 with results shown in section 4. The analysis requires specification of a base altitude level (pressure in mb). Cloud and PWV above this level (or the surface if higher) will be computed. Therefore it is important that the user is aware of the relationship between the actual altitude of locations, the digital elevation model altitudes as used in the analysis and the base altitude level to ensure that results are interpreted correctly.

Additional caution must be exercised when analysing and comparing specific sites. The software uses the NCEP-NCAR reanalysis data to define the vertical profile of temperature that is used to determine the threshold temperature for cloud detection (T_r) (see section 3). The vertical and horizontal resolution of these data is fairly crude. To analyse site conditions it is often preferable to use upper-air temperature data from a nearby rawinsonde station since these have higher vertical resolution and are more representative of local conditions. Also the actual site altitude should be used rather than that from the digital elevation model. In addition the effective spatial resolution of the NCEP-NCAR data may be poor in some data-sparse areas (eg. over the Sahara desert). Therefore the user must be cautious when comparing sites in areas with good data coverage to sites in areas with poor data coverage.

The factors mentioned above show that the proper application of the software requires a certain level of knowledge of how the software works and also the meteorological background required to interpret the output correctly. Regarding the software package, the following disclaimer should therefore be noted by all users (This disclaimer also appears in the software):

Disclaimer: *This software was prepared under contract between D. Andre Erasmus, Ph.D., Certified Consulting Meteorologist (henceforth, the Contractor) and European Southern Observatory (ESO). It is understood that ESO may make this software available to other parties under existing ESO member nation agreements. The proper use of this software and its output products requires a certain level of*

knowledge of how the software works and also the physical (meteorological) principles incorporated therein. Contact the Contractor (erasmus@saao.ac.za) for more information. The Contractor is not responsible for the erroneous use of this software, incorrect interpretation of the output or the outcome of decisions made on the basis of the output.

7. References

Erasmus, D.A., 2004: An Analysis and Comparison Of Satellite-Observed Cloud Cover and Water Vapor At Hanle, India and Yanbajing, Tibet. Experimental Particle Physics and High Energy Astrophysics Group.The Max-Planck-Institute for Nuclear Physics Heidelberg. Final Report. 31 January, 2004.

Erasmus, D.A., 2005: Precipitable Water Vapour at SKA Telescope Candidate Sites: Derivation from rawinsonde data and a discussion of alternative measurement methods. International SKA Project Memorandum 59, January 2005. (www.skatelescope.org/PDF/memos/59_Erasmus.pdf)

Erasmus, D.A., D.S. Maartens and R. van Rooyen, 2003: Operational Forecasts of Cloud Cover and Water Vapour For ESO Observatories: Maintenance, Revision of the Movement Algorithm and Development of a Transparency Index. Purchase Order 65015/ODG/01/8636/CNI/LET

Erasmus, D.A. and M. Sarazin, 2000: Forecasting Precipitable Water Vapor and Cirrus Cloud Cover For Astronomical Observatories: Satellite image processing guided by synoptic model dissemination data. SPIE Conference on Image and Signal Processing for Remote Sensing IV. Paper SPIE-4168, Barcelona. 25-29 September, 2000.

Erasmus, D.A. and M. Sarazin, 2002: Utilizing Satellite Data For Evaluation and Forecasting Applications At Astronomical Sites. IAU Technical Workshop: Astronomical Site Evaluation in the Visible and Radio Range. Marrakesh, Morocco, 13-17 November, 2000. Astronomical Society of the Pacific Conference Series. Vol. 266, 310-326.

Erasmus, D.A., and C.A. van Staden, 2001: A Satellite Survey of Water Vapour and Cloud Cover in Northern Chile. Final Report. Cerro-Tololo Inter-American Observatory.

Erasmus, D.A., and C.A. van Staden, 2002: A Satellite Survey of Water Vapor and Cloud Cover in the South-western U.S.A. and Northern Mexico. Final Report. The CELT Project and Aura Inc. 54pp.

Erasmus, D.A., and C.A. van Staden, 2003: A Comparison of Satellite-Observed Cloud Cover and Water Vapor at Mauna Kea and Selected Sites in Northern Chile, the Southwestern U.S.A. and Northern Mexico. Final Report. 31 August, 2003. New Initiatives Office, Aura Inc. 75pp.

Erasmus, D.A., and R. van Rooyen, 2004: A Satellite Survey Of Cloud Cover and Water Vapour In Morocco and Southern Spain and a Verification Using La Palma Ground-based Observations. Interim Report, 19 November, 2004. 23pp.

Evans, D.W., 2005: Personal Communication

Kistler, R, E. Kalnay, W. Collins, S. Saha, G. White, J. Woollen, M. Chelliah, W. Ebisuzaki, M. Kanamitsu, V. Kousky, H. van den Dool, R. Jenne, and M. Fiorino, 2001: The NCEP-NCAR 50-Year Reanalysis: Monthly Means CD-ROM and Documentation. *Bull. Amer. Meteor. Soc.*, 82, 2, 257-267

Rao, P.K., S.J. Holmes, R.K. Anderson, J.S. Winston and P.E. Lehr, Eds., 1990: *Weather Satellites: Systems, Data and Environmental Applications*. American Meteorological Society, Boston, 503pp.

Roca, R., H. Broniez, L. Picon and M. Desbois, 2003: Free Tropospheric Humidity Observations from METEOSAT Water Vapour Data. Paper J3.7, AMS proceedings.

Sarazin, M. 1991: Air temperature cycles at Paranal. VLT-TRE-ESO-17440-0001, Revision 1, March 21, 1991.

Soden, B.J., and F.P. Bretherton, 1993: Upper tropospheric relative humidity from the GOES 6.7μm channel: Method and climatology for July 1987. *J. Geophys. Res.* 96, 16669-16688.

Soden, B.J., and F.P. Bretherton, 1996: Interpretation of TOVS water vapor radiances in terms of layer-average relative humidities: Method and climatology for the upper, middle and lower troposphere. *J. Geophys. Res.* 101, 9333-9343.

van Rooyen, R. and D.A. Erasmus, 2004: A Satellite Survey Of Cloud Cover and Water Vapour In Morocco and Southern Spain and a Verification Using La Palma Ground-based Observations – Technical Supplement. 19 November, 2004. 80pp.

APPENDIX A

Scatter plots and regression relationships between water vapour channel brightness temperature (T_{wv}) and UTH for Meteosat-5 by month (01-12).

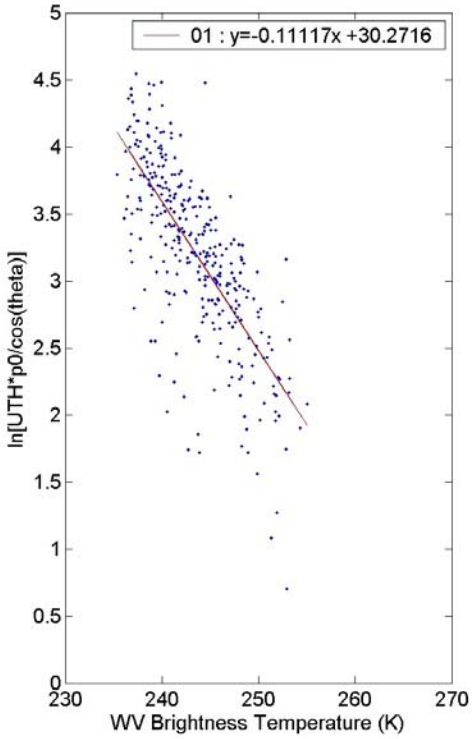

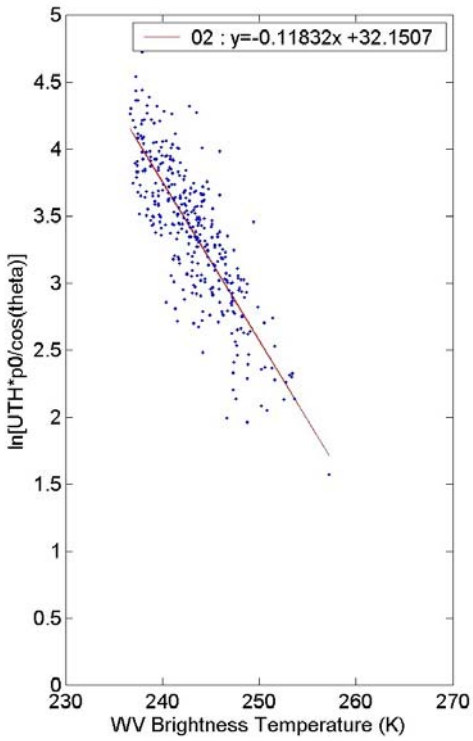

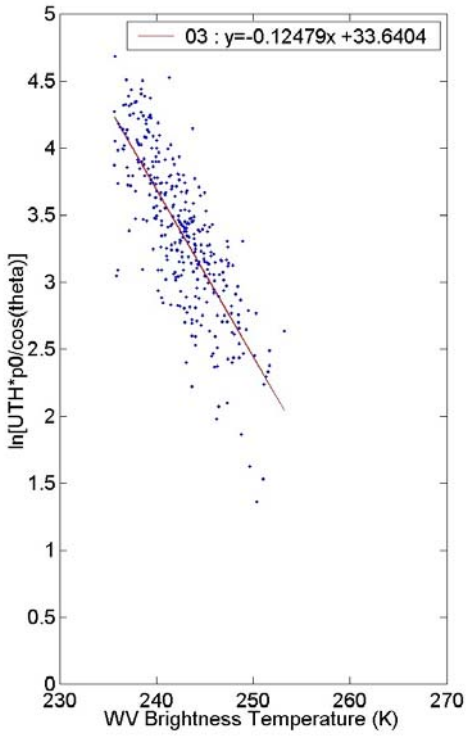

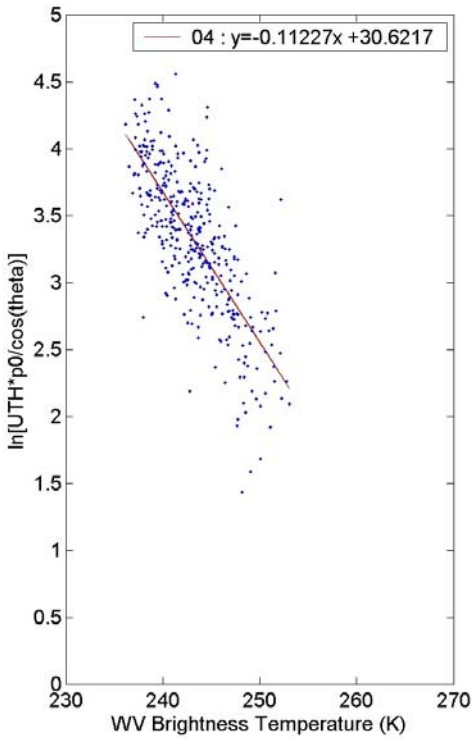

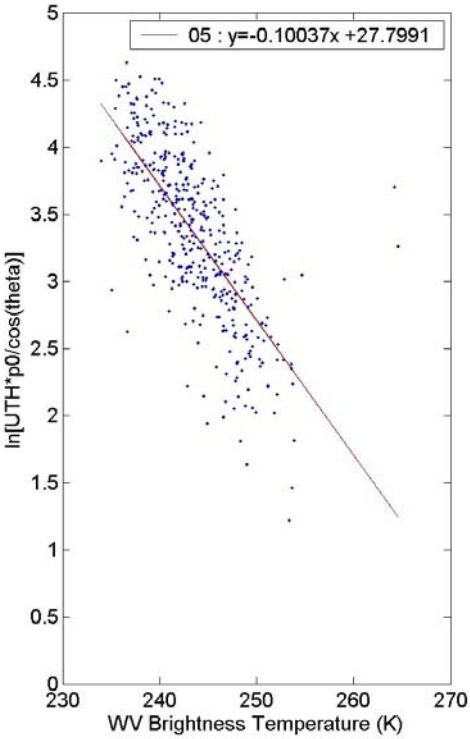
05 : y=-0.10037x +27.7991
ln[UTH*p0/cos(theta)]
WV Brightness Temperature (K)

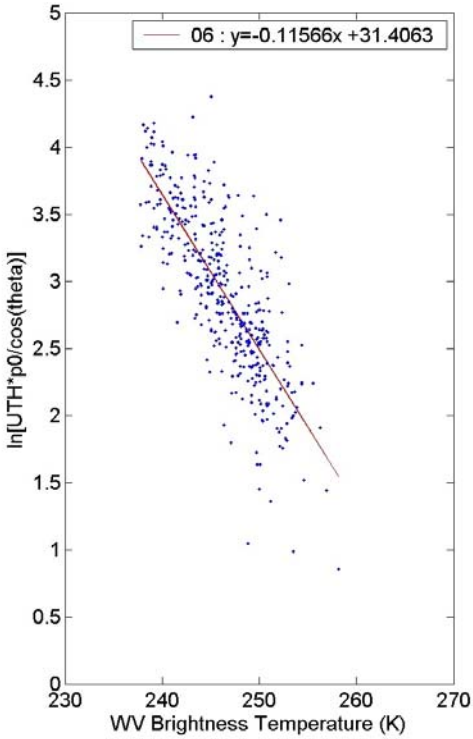
06 : y=-0.11566x +31.4063
ln[UTH*p0/cos(theta)]
WV Brightness Temperature (K)

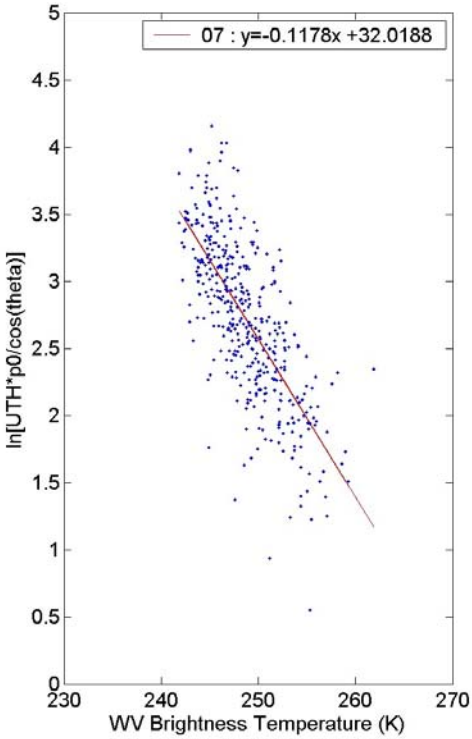
07 : y=-0.1178x +32.0188
ln[UTH*p0/cos(theta)]
WV Brightness Temperature (K)

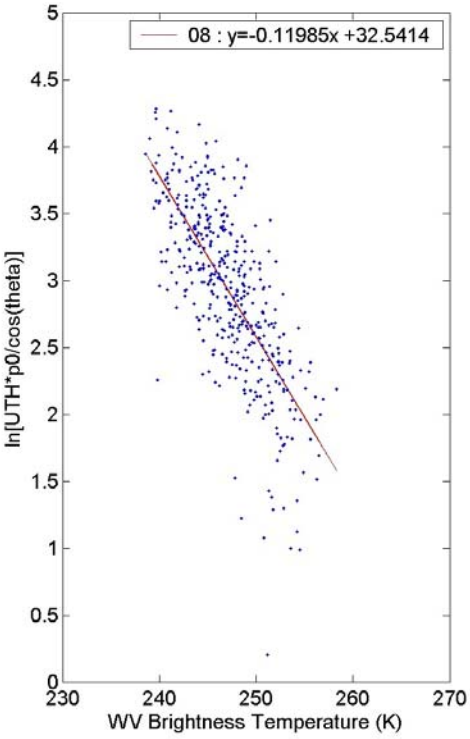
08 : y=-0.11985x +32.5414
ln[UTH*p0/cos(theta)]
WV Brightness Temperature (K)

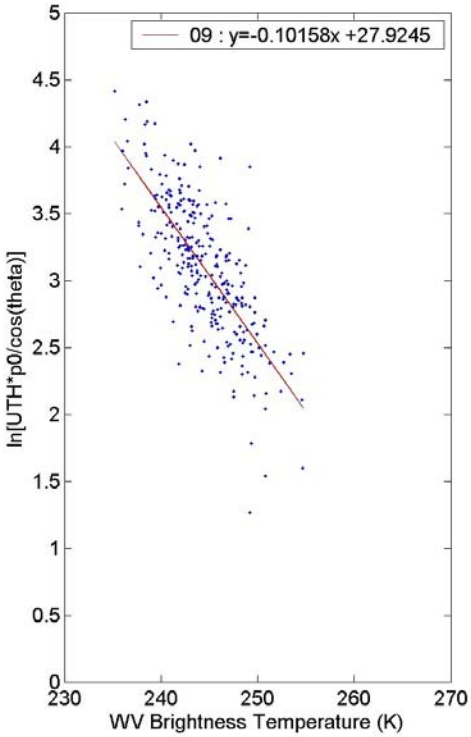
09 : y=-0.10158x +27.9245
ln[UTH*p0/cos(theta)]
WV Brightness Temperature (K)

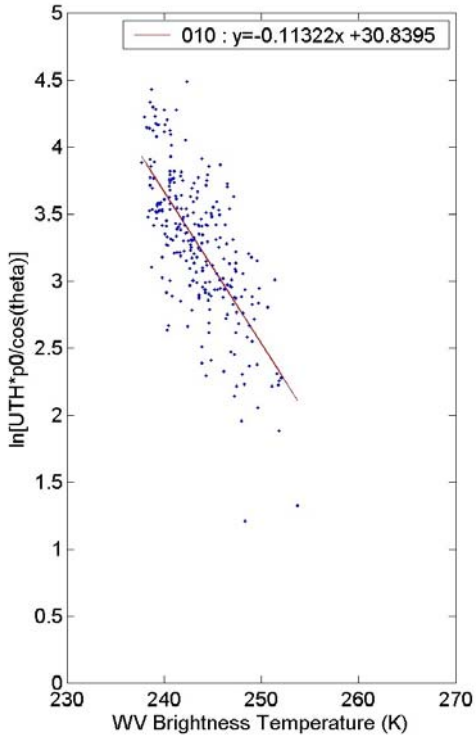
010 : y=-0.11322x +30.8395
ln[UTH*p0/cos(theta)]
WV Brightness Temperature (K)

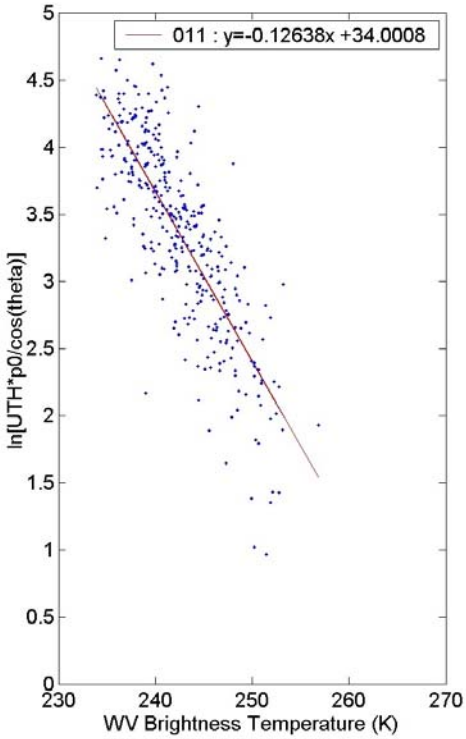
011 : y=-0.12638x +34.0008
ln[UTH*p0/cos(theta)]
WV Brightness Temperature (K)

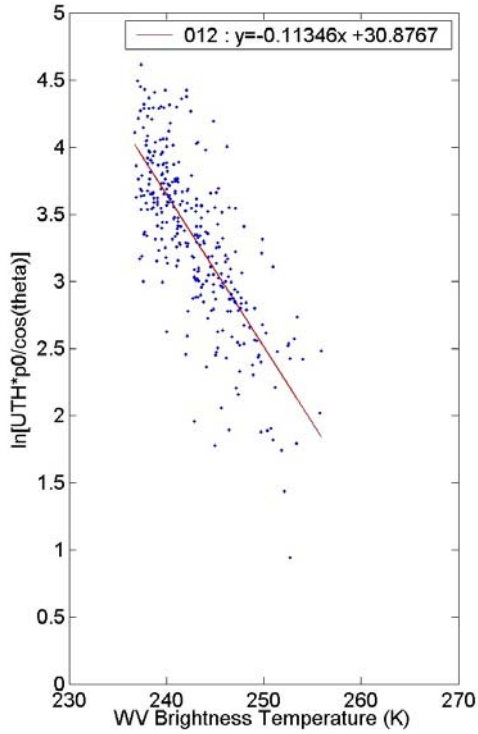
012 : y=-0.11346x +30.8767
ln[UTH*p0/cos(theta)]
WV Brightness Temperature (K)

APPENDIX B

Time series plots of ORM nightly clear/photometric fraction as determined from satellite data and ground-based observations of atmospheric extinction made by the CMT (see section 5.). Plots are shown by year for 2000, 2001 and 2002. In the plots for the CMT photometric fraction, (Obs ~ NL) indicates nights where the observation period was at least 80% of the night length.